The Astrophysical Journal, 750:37 (17pp), 2012 May 1 doi:10.1088/0004-637X/750/1/37

COSMOS: STOCHASTIC BIAS FROM MEASUREMENTS OF WEAK LENSING AND GALAXY CLUSTERING

Eric Jullo[1,2], Jason Rhodes[1], Alina Kiessling[3], James E. Taylor[4], Richard Massey[3], Joel Berge[5], Carlo Schimd[2], Jean-Paul Kneib[2], and Nick Scoville[6]
[1] Propulsion Laboratory, California Institute of Technology, Pasadena, CA 91109, USA; eric.jullo@oamp.fr
[2] Laboratoire d'Astrophysique de Marseille, Université de Provence, CNRS, 13388 Marseille CEDEX 13, France
[3] Institute for Astronomy, Blackford Hill, Edinburgh EH9 3HJ, UK
[4] Department of Physics and Astronomy, University of Waterloo, 200 University Avenue West, Waterloo, Ontario N2L 3G1, Canada
[5] Institute of Astronomy, Department of Physics, ETH Zurich CH-8093, Switzerland
[6] Astronomy Department, California Institute of Technology, MC 105-24, 1200 East California Boulevard, Pasadena, CA 91125, USA
Received 2011 March 25; accepted 2012 February 22; published 2012 April 13

ABSTRACT

In the theory of structure formation, galaxies are biased tracers of the underlying matter density field. The statistical relation between galaxy and matter density field is commonly referred to as galaxy bias. In this paper, we test the linear bias model with weak-lensing and galaxy clustering measurements in the 2 deg^2 COSMOS field. We estimate the bias of galaxies between redshifts $z = 0.2$ and $z = 1$ and over correlation scales between $R = 0.2\,h^{-1}$ Mpc and $R = 15\,h^{-1}$ Mpc. We focus on three galaxy samples, selected in flux (simultaneous cuts $I_{814W} < 26.5$ and $K_s < 24$) and in stellar mass ($10^9 < M_* < 10^{10}\,h^{-2}\,M_\odot$ and $10^{10} < M_* < 10^{11}\,h^{-2}\,M_\odot$). At scales $R > 2\,h^{-1}$ Mpc, our measurements support a model of bias increasing with redshift. The Tinker et al. fitting function provides a good fit to the data. We find the best-fit mass of the galaxy halos to be $\log(M_{200}/\,h^{-1}\,M_\odot) = 11.7^{+0.6}_{-1.3}$ and $\log(M_{200}/\,h^{-1}\,M_\odot) = 12.4^{+0.2}_{-2.9}$, respectively, for the low and high stellar-mass samples. In the halo model framework, bias is scale dependent with a change of slope at the transition scale between the one and the two halo terms. We detect a scale dependence of bias with a turndown at scale $R = 2.3 \pm 1.5\,h^{-1}$ Mpc, in agreement with previous galaxy clustering studies. We find no significant amount of stochasticity, suggesting that a linear bias model is sufficient to describe our data. We use *N*-body simulations to quantify both the amount of cosmic variance and systematic errors in the measurement.

Key words: cosmology: observations – gravitational lensing: weak – large-scale structure of universe

Online-only material: color figures

1. INTRODUCTION

In the theory of structure formation, galaxies form in dark matter overdensities. However, the distribution of galaxies does not perfectly match the underlying matter distribution, and the relation between the two is called galaxy bias.

The galaxy bias relation $\delta_g = f(\delta)$ relates the matter density contrast δ to the galaxy density contrast δ_g. The density contrast δ is defined as the ratio between the local and the mean densities $\delta \equiv \rho/\bar{\rho} - 1$. To first order, the galaxy bias relation $\delta_g = b\delta$ is parameterized by the bias parameter b. However, the stochasticity in the physical processes of galaxy formation might introduce some stochasticity in the galaxy bias relation. The amount of stochasticity can be measured with the correlation coefficient r defined as the ratio between the covariance and the variance of the density contrasts δ and δ_g, $r = \langle\delta_g\delta\rangle/\sqrt{\langle\delta_g^2\rangle\langle\delta^2\rangle}$. A correlation coefficient $r = 1$ means that the bias relation is perfectly linear, whereas $0 < r < 1$ suggests stochasticity and/or nonlinearity (Dekel & Lahav 1999). We do not expect the bias relation to be anti-correlated with $r < 0$ or $b < 0$ (i.e., galaxy clustering decreases when matter clustering increases).

Bias varies for different galaxy populations. Galaxy biasing is known to be larger for luminous, red, and high-redshift galaxies (Marinoni et al. 2005; Meneux et al. 2006; Coil et al. 2008; Zehavi et al. 2011). Bias also varies with scale, but differently for different galaxy types and luminosity (Cresswell & Percival 2009; Ouchi et al. 2005; McCracken et al. 2010). In the halo-model framework, the scale dependence of bias is explained as the transition from a small-scale regime where galaxies are in the same halo of dark matter to a large-scale regime where galaxies are in two different halos (see, e.g., Zheng et al. 2009, for a recent discussion). The scale dependence of bias therefore tells us about the dark matter halo properties around galaxies.

Tegmark & Bromley (1999) first measured bias stochasticity in the Las Campanas Redshift Survey. At the same time, simulations started to predict stochasticity, as well as scale and redshift dependence in the bias relation due to physical processes (Blanton et al. 1999; Somerville et al. 2001; Yoshikawa et al. 2001). In the 2dF Galaxy Redshift Survey, Wild et al. (2005) used the count-in-cell technique to measure the nonlinearity and stochasticity of the bias relation for red/early-type and blue/late-type galaxies at redshift $z < 0.114$. For both categories, they found more stochasticity at scale $R = 10$ Mpc than at scale $R = 45$ Mpc. Recent results from simulations also predict an increasing amount of stochasticity at smaller scales (Baldauf et al. 2010).

The correlation coefficient is at the same time an estimate of stochasticity and nonlinearity. In the zCOSMOS redshift survey (Lilly et al. 2009), Kovač et al. (2011) found nonlinearity to contribute less than ∼0.2% to the bias relation for luminosity-selected galaxies ($M_B < -20 - z$). Therefore, in the following, we will assume that the correlation coefficient r mostly quantifies bias stochasticity. With respect to the bias parameter b, Kovač et al. (2011) found the bias relation to be scale independent (SI) between scales $R = 8\,h^{-1}$ Mpc and $R = 10\,h^{-1}$ Mpc and redshift dependent between redshifts $z = 0.4$ and $z = 1$.

In this work, we measure galaxy bias with a technique proposed by Schneider (1998) based on galaxy clustering and weak lensing. In short, weak lensing is used to derive matter clustering from the shape of background galaxies, which is

then compared to the galaxy clustering to infer the bias. Van Waerbeke et al. (1999) emphasized the potential of this technique with analytical calculations for surveys with various depths and areas, and Hoekstra et al. (2001, 2002) applied it to the 50.5 deg^2 of the Red sequence Cluster Survey (RCS) and VIRMOS-DESCART survey. They measured the linear bias parameter b and the correlation coefficient r for a flux-limited galaxy sample ($19.5 < R_C < 21$) at redshift $\bar{z} \simeq 0.35$ and on scales between $R = 0.2$ and $9.3\,h_{50}^{-1}$ Mpc. They found strong evidence that both b and r change with scale, and $r \sim 0.57$ at $1\,h_{50}^{-1}$ Mpc, which suggests a significant degree of stochasticity and/or nonlinearity in their sample of galaxies. Simon et al. (2007) applied the same technique to the 15 deg^2 of the GaBoDS survey for three flux-limited galaxy samples in the R band, at redshift $\bar{z} = 0.35$, 0.47, and 0.61. They also found bias to be scale dependent (SD), with an increasing amount of bias at small scales. In addition, they found the bias parameters b and r to be redshift independent within statistical uncertainties, with $r \sim 0.6$. Finally, Sheldon et al. (2004) performed a comparable study in the 3800 deg^2 of the Sloan Digital Sky Survey (SDSS), with volume- and magnitude-selected galaxies ($0.1 < z < 0.174$ and $-23.0 < M_r - 5\log h < -21.5$). In agreement with Hoekstra et al. (2002), they found the ratio b/r to be SI between 0.4 and 6.7 h^{-1} Mpc, with $(b/r) = (1.3 \pm 0.2)(\Omega_m/0.27)$ for a flux-limited galaxy sample. In fact, the Hoekstra et al. (2002) results suggested that the respective scale dependence of b and r conspires to produce an SI ratio b/r. In summary, the consistent value of $r < 1$ found in all these studies suggests some degree of stochasticity in the investigated galaxy samples.

In this work, we study the bias of galaxies in the 2 deg^2 of the COSMOS field. We test the linear bias model and its dependence on scale and redshift. For two galaxy samples selected in stellar mass and one sample selected in flux, we measure bias on scales between $0.2\,h^{-1}$ Mpc and $15\,h^{-1}$ Mpc and redshifts between $z = 0.2$ and $z = 1$. COSMOS is ideal to perform this study because accurate stellar mass has been measured up to redshift $z \sim 1.2$ (Bundy et al. 2010) and photometric redshifts up to redshift $z \sim 4$ (Ilbert et al. 2009). In addition, with the high-resolution images from the Advanced Camera for Survey aboard the *Hubble Space Telescope* (ACS/*HST*), we can precisely measure the shape of more than 200,000 galaxies. Measuring the shape of galaxies at redshift $z > 2$ is crucial for weak lensing to allow accurate determination of the matter density up to redshift $z \sim 1$. In Section 2, we present the COSMOS survey, our lensing catalog, and our selection of foreground galaxies for which we want to measure the bias. In Section 3, we describe the lensing formalism used in this paper. In Section 4, we present a set of simulations we use to quantify the impact of cosmic variance. In Section 5, we show our results, and we go on to discuss some possible systematic errors in Section 6. We conclude in Section 7.

In this paper, we assume the WMAP7 (Komatsu et al. 2011) cosmological parameters $\Omega_m = 0.272$, $\Omega_\Lambda = 0.728$, $\Omega_b = 0.0449$, $\sigma_8 = 0.809$, $n = 0.963$, $\omega_0 = -1$, and $h = 0.71$.

2. DATA

2.1. General Properties

The COSMOS field is a 1.64 deg^2 patch of sky close to the equator ($\alpha = 10^{\rm h}00^{\rm m}28^{\rm s}$., $\delta = +2^\circ12'21''$.). It was imaged with ACS/*HST* during cycles 12–13 (Scoville et al. 2007; Koekemoer et al. 2007). An intensive follow-up from UV to IR was conducted by several ground-based and space-based telescopes. In this study, we take advantage of the spatial resolution of the ACS imaging to measure the shape of the galaxies and of the multi-filter ground-based imaging to derive accurate photometric redshifts (Ilbert et al. 2009).

2.2. Lensing Catalog

We use an updated version of the lensing catalog presented in Leauthaud et al. (2007). In this new catalog, raw ACS/f814w images have been corrected for the Charge Transfer Inefficiency effect using the algorithm described in Massey et al. (2010). Objects are detected with the "hot-cold" technique described in Leauthaud et al. (2007), i.e., SExtractor (Bertin & Arnouts 1996) is run twice: first to detect extended objects and then compact objects. Regions contaminated by bright stars or satellite trails are masked out. Point sources and spurious detections are discarded as detailed in Leauthaud et al. (2007). The catalog is complete up to magnitude MAG_AUTO = 26.5 in the ACS/f814w band (hereafter I_{814W}).

Galaxy ellipticities are measured with the RRG algorithm described in Rhodes et al. (2000) and calibrated with the same shear calibration as in Leauthaud et al. (2007). In our final source catalog, we make the cuts on size $d > 1.6$ times the point-spread function size and S/N > 4.5 as in Leauthaud et al. (2007). We also remove galaxies with more than one peak in their photometric redshift probability distribution function (pdf) or galaxies masked in the Subaru imaging. This way, we obtain an average redshift error $\sigma_z/(1+z) < 0.05$. Our source catalog with good shapes and redshifts contains 210,477 galaxies, which yields a density of 36 galaxies per square arcminute. As in Massey et al. (2007b), we assign to every source galaxy an inverse variance weight w aimed at maximizing the S/N and calculate from the galaxy apparent magnitude

$$w = \frac{1}{\sigma_\epsilon^2 + 0.1}\,, \tag{1}$$

where the observational noise (pixellation, shot noise, etc.) is well approximated by the following function of the galaxy apparent magnitude in the I_{814W} band:

$$\sigma_\epsilon = 0.32 + 0.0014(\text{MAG\_AUTO} - 20)^3\,. \tag{2}$$

The second term 0.1 represents the variance of the intrinsic shape noise, which was found to be pretty constant in Leauthaud et al. (2007). Note that the power of 2 was omitted as a typo in Massey et al. (2007b).

2.3. Foreground and Background Galaxy Catalogs

2.3.1. Catalog Cuts by Redshift

In this work, we want to study the evolution of galaxy bias as a function of redshift and scale. Bias is computed from the ratio of galaxy and matter clustering in bins of redshift. To ease the interpretation of the bias results later on, we choose to define foreground galaxy samples with redshift distributions matching the redshift distribution of the matter that most efficiently perturbs the background galaxy shapes through weak lensing. Typically, the matter that lies halfway between us and the background galaxies is the one that most efficiently perturbs their shape. We show in Section 6 that a mismatch in redshift can change the estimated bias.

We create three bins B1, B2, and B3 of background sources. We set the bin limits to $z = 0.3$, 0.8, 1.4, and 4, so that the

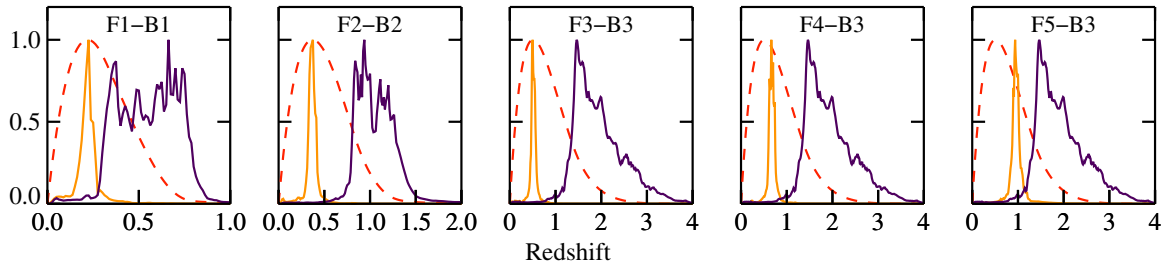

Figure 1. Redshift distributions of the three background catalogs B1–B3 (purple/dark line) and the five foreground catalogs F1–F5 (yellow/light line). The normalized lensing efficiency curves (red dashed lines) give the location where the matter most efficiently perturbs the shape of the background galaxies.
(A color version of this figure is available in the online journal.)

Table 1
Redshift Range and Number of Galaxies per Foreground and Background Bins

Bin	Redshift Range	Stellar Mass Range $[h_{72}^{-2}\,M_\odot]$		All
		$10^9 \rightarrow 10^{10}$	$10^{10} \rightarrow 10^{11}$	
F1	[0.17, 0.27]	1,298	644	7,920
F2	[0.32, 0.42]	3,151	1,770	13,898
F3	[0.47, 0.57]	3,215	1,456	11,256
F4	[0.60, 0.75]	7,776	3,899	22,958
F5	[0.87, 1.07]	11,828	6,223	27,911
B1	[0.3, 0.8]	...	...	63,529
B2	[0.8, 1.4]	...	...	70,157
B3	[1.4, 4.0]	...	...	59,056

number of galaxies and signal to noise in each bin are similar. We assign a galaxy with redshift $z \pm \sigma_{68\%}$ to a particular redshift bin with limits $z_{\rm low}$ and $z_{\rm high}$ if $z - \sigma_{68\%} > z_{\rm low}$ and $z + \sigma_{68\%} < z_{\rm high}$. The values of z and $\sigma_{68\%}$ are estimated from the photometric redshift likelihoods. The number of galaxies per bin is reported in Table 1.

For each background bin, we compute the lensing efficiency. The lensing efficiency is a calculation based on the redshift distribution of the background galaxies in comoving coordinates $p_b(w) = p_b(z)dz/dw$ and of the cosmological parameters. We use it as a weighting function in the following to project the three-dimensional matter power spectrum along the line of sight. The lensing efficiency as a function of the comoving distance to the lens is defined as

$$g(w) = \frac{3\Omega_m H_0^2 f_K(w)}{2c^2 a(w)} \int_w^{w_h} dw'\; p_b(w') \frac{f_K(w - w')}{f_K w'}, \quad (3)$$

where the functions $a(w)$ and $f_K(w)$ are, respectively, the comoving scale factor and the comoving angular distance. We find the lensing efficiency curves to peak at redshifts $z_{\rm B1} = 0.22$, $z_{\rm B2} = 0.37$, and $z_{\rm B3} = 0.51$.

Next, we create five bins of foreground galaxies. For the first three bins, we adjust their centers to match the peaks of the three lensing efficiencies. Then, we adjust their width so that the signal to noise of the galaxy–galaxy cross-correlation measurements is the largest. Too broad bins increase the mixing of angular and physical scales, and too narrow bins increase shot noise. Bins must also be broad enough, so that we can use the Limber approximation to compute the theoretical signal. Indeed, the Limber approximation breaks down at large scales for too narrow redshift bins. Simon (2007) computed the minimal bin width as a function of scale and redshift, beyond which the Limber approximation becomes inaccurate by more than 10%. To minimize the impact of this issue, we fix the bin width so that we reach 10% inaccuracy at 100 arcmin, i.e., twice the largest scale at which we compute the correlation functions. In summary, we obtain three foreground bins with limits $0.17 < z_{\rm F1} < 0.27$, $0.32 < z_{\rm F2} < 0.42$, and $0.47 < z_{\rm F3} < 0.57$. To these three foreground bins, we add two extra bins to probe the bias at higher redshift $0.60 < z_{\rm F4} < 0.75$ and $0.87 < z_{\rm F5} < 1.07$. Finally, we assign the foreground galaxies to their respective bins using the same criteria we used for the background sources and compute $p_f(z)$, the redshift distribution of the foreground bins. Again, we will use these redshift distributions as weighting functions to project the three-dimensional matter power spectrum along the line of sight and compute the different estimators presented below.

Note here three important points regarding our analysis. First, we compute the redshift distribution of the galaxies that fall in the foreground and background redshift bins $p_f(z)$ and $p_b(z)$ by summing their redshift posterior pdf $p^{(i)}(z)$. The redshift distributions $p_f(z)$ and $p_b(z)$ and the lensing efficiency curves are shown in Figure 1. Summing the redshift pdfs instead of building histograms of the individual redshift estimates has several advantages: (1) it helps to deal with skewed pdfs, and (2) it tells us about the probability of having galaxies outside a redshift bin. In spite of our cuts in redshift, we still find that 30% of the galaxies are probably outside the redshift limits of their respective redshift bins. If instead we choose to cut galaxies at $3\sigma_{68\%}$ from the redshift bin limits, we only decrease this probability to 28%. (3) It gives us theoretical predictions that better reproduce the measurements. Summing the pdfs produces redshift distributions with tails falling outside the redshift bin limits. As a result, we predict projected power spectra with larger amplitudes at small and large scales. They reproduce better measurements.

Second, we must emphasize that the redshift distributions we obtain are weighting functions that we use to project the three-dimensional matter power spectrum along the line of sight and predict the behavior of several estimators. In particular, we use the lensing efficiency in place of the lensing-effective matter distribution. The latter would be the true matter redshift distribution multiplied by the lensing efficiency. Nonetheless, by averaging over many lines of sight, we expect the lensing efficiency to approximate the lensing-effective matter distribution and thus produce accurate predictions.

Third, the centers of foreground bins F4 and F5 do not perfectly match the peak of the lensing efficiency for catalog B3. In Section 6, we show how such a mismatch can alter the bias measurements. We show that the effects are particularly severe at small scales in the nonlinear regime. Fortunately for bins F4 and F5 most of the angular scales we probe correspond

to physical scales in the quasi-linear and linear regime. Since the scale dependence of the bias in the linear regime is small, the effect of mismatch in redshift will be small.

2.3.2. Catalog Cuts by Flux and Stellar Mass

In order to investigate the dependence of bias with stellar mass, we further partition our foreground catalogs into one flux-selected and two stellar-mass-selected catalogs. The COSMOS catalog for the foreground galaxies is complete up to $I_{814W} < 26.5$ and $K_s < 24$ in AB magnitude (Capak et al. 2007; Ilbert et al. 2009; Leauthaud et al. 2007). The limit in K_s band is more conservative and comes from estimating the observed magnitude of a maximal M_*/L stellar population model with solar metallicity, no dust, and a $\tau = 0.5$ Gyr burst of star formation at redshift $z_{\rm form} = 5$ (Leauthaud et al. 2012). Bundy et al. (2010) computed the 80% completeness in stellar mass for magnitude-selected galaxies $K_s < 24$ and $I_{814W} < 26.5$. They found the 80% completeness lower limits in $\log M_*/M_\odot$ to be 8.8, 9.3, 9.7, and 10.0 for their redshift bins [0.2, 0.4], [0.4, 0.6], [0.6, 0.8], and [0.8, 1.0]. In order to have enough galaxies per bin, we bin in the two stellar mass bins $10^9 < M_* < 10^{10}\, h_{72}^{-2}\, M_\odot$ and $10^{10} < M_* < 10^{11}\, h_{72}^{-2}\, M_\odot$. Our low stellar-mass galaxy samples are therefore more than 80% complete in all redshift bins, and our high stellar-mass galaxy sample is more than 80% complete in bins F1 and F2, about 80% complete in bin F3, and less than 80% complete in bins F4 and F5. For comparison, the mean stellar masses in our flux-limited galaxy samples in bins F1, F2, F3, F4, and F5 are 9.6, 9.7, 9.8, 10.0, and 10.1 in units of $\log(M_*/h_{72}^{-2}\, M_\odot)$.

3. LENSING METHOD

In gravitational lensing theory, the mass of foreground structures locally perturbs spacetime, deviates the path of light rays coming to us from background galaxies, and distorts their intrinsic shape. By analyzing the shape of many background galaxies, it is therefore possible to infer the properties of the intervening structures. For instance, the correlation of ellipticity measurements of background galaxies tells us about the clustering of the foreground structures. As such, gravitational lensing is a direct probe of the matter density field projected along the line of sight. Perturbations of the background galaxy shapes are of two kinds. The convergence κ quantifies the amount of isotropic amplification, and the shear, $\gamma = \gamma_1 + i\gamma_2$, quantifies the amount of stretch along some direction.

If we consider a sample of background galaxies with lensing efficiency as a function of redshift $g(z)$, the convergence and shear produced by the matter along the line of sight, expressed in terms of density contrast δ, are

$$\kappa(\theta) = \int_0^{w_h} dw\, g(w)\delta(f_K(w)\theta, w)\,, \tag{4}$$

$$\gamma(\theta) = -\frac{1}{\pi}\int d^2\theta'\,\kappa(\theta'-\theta)\frac{1}{(\theta_1'-\theta_2')^2}\,. \tag{5}$$

Schneider et al. (1998) introduce the mass aperture statistic $M_{\rm ap}$ defined as

$$\mathrm{M_{ap}}(\theta) = \int_0^{\theta} d^2\vartheta\; U(|\vartheta|)\kappa(\vartheta)\,, \tag{6}$$

where the integral extends over a disk of angular radius θ. $U(\theta)$ is a compensated weight function that vanishes for $\vartheta > \theta$. In a similar manner, the aperture number count of galaxies at a scale θ is defined as

$$N(\theta) = \int_0^{\theta} d^2\vartheta\; U(|\vartheta|)\delta_g(\vartheta), \tag{7}$$

where $U(\vartheta)$ is the same function as above and $\delta_g(\theta)$ is the galaxy density contrast.

3.1. Variance Aperture Statistics

Schneider (1998) and van Waerbeke (1998) developed a formalism based on aperture statistics to measure the dependence of bias with scale. They define the following aperture statistics from the auto- and cross-power spectra of galaxies and matter $P_n(\ell)$, $P_\kappa(\ell)$, and $P_{n\kappa}(\ell)$, respectively,

$$\langle \mathcal{N}^2(\theta)\rangle = 2\pi\int_0^\infty d\ell\;\ell\;P_n(\ell)\,[I(\ell\theta)]^2\;, \tag{8}$$

$$\left\langle M_{\rm ap}^2(\theta)\right\rangle = 2\pi\int_0^\infty d\ell\;\ell\;P_\kappa(\ell)\,[I(\ell\theta)]^2\;, \tag{9}$$

$$\langle \mathcal{N}(\theta)M_{\rm ap}(\theta)\rangle = 2\pi\int_0^\infty d\ell\;\ell\;P_{n\kappa}(\ell)\,[I(\ell\theta)]^2\;. \tag{10}$$

The filter $I(x)$ is defined as (Schneider et al. 1998; Hoekstra et al. 2002; Simon et al. 2007)

$$I(x) = \frac{12}{\pi}\frac{J_4(x)}{x^2}, \tag{11}$$

where $J_4(x)$ is the Bessel function of order 4. This filter is a narrowband filter, which peaks at $x \sim 4.25$. The power spectra $P_n(\ell)$, $P_\kappa(\ell)$, and $P_{\kappa n}(\ell)$ are derived from the three-dimensional matter power spectrum $P_m(k, w)$ projected along the line of sight, weighted by the functions $g(w)$, $p_f(w)$, or $p_f(w)g(w)$, and altered by the bias parameters b and r. Their respective analytical expressions are

$$P_n(\ell) = \int_0^{w_h} dw\,\frac{[p_f(w)]^2}{[f_K(w)]^2}b^2 P_m\left(\frac{\ell}{f_K(w)}, w\right), \tag{12}$$

$$P_\kappa(\ell) = \int_0^{w_h} dw\,\frac{[g(w)]^2}{[f_K(w)]^2}P_m\left(\frac{\ell}{f_K(w)}, w\right), \tag{13}$$

and

$$P_{\kappa n}(\ell) = \int_0^{w_h} dw\,\frac{g(w)p_f(w)}{[f_K(w)]^2}br\,P_m\left(\frac{\ell}{f_K(w)}, w\right). \tag{14}$$

We use the Limber approximation here to simplify the integrals.

The technique developed in this paper is powerful because all the power spectra are filtered by the same narrowband filter $I(x)$. In contrast, the estimators ξ_+, ξ_-, $\omega(\theta)$, and $\langle\gamma_t\rangle$ involve four different filters (see Appendix B). Combining them directly would lead to a mixing of modes in Fourier space and would hamper the interpretation.

3.2. Bias Measured from Aperture Statistics

The bias parameters b and r are defined as ratios of the variance aperture statistics

$$b(\theta) = f_1(\theta, \Omega_m, \Omega_\Lambda) \times \sqrt{\frac{\langle \mathcal{N}^2(\theta)\rangle}{\left\langle M_{\rm ap}^2(\theta)\right\rangle}}\,, \tag{15}$$

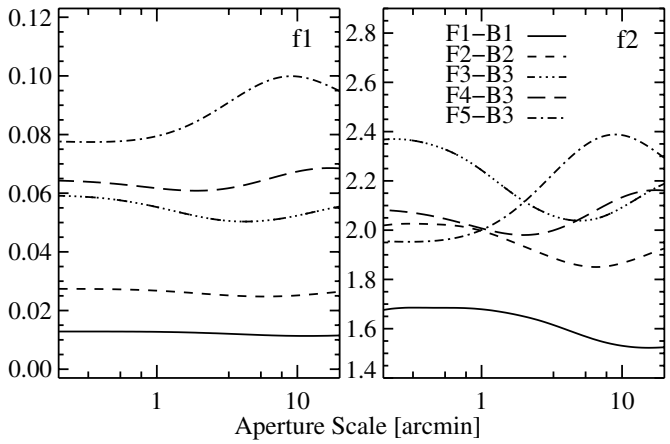

Figure 2. Bias calibration factors $f1$ and $f2$ used to calibrate b and r, respectively. We compute them assuming a Smith et al. (2003) nonlinear power spectrum with unbiased foreground galaxies ($b = r = 1$), an Eisenstein & Hu (1999) transfer function, and the WMAP7 cosmological parameters (Komatsu et al. 2011). Deviations from a straight line are due to mismatches in Fourier space of scales probed by the galaxy and the matter aperture statistics $\langle \mathcal{N}^2(\theta)\rangle$ and $\langle M_{\rm ap}^2(\theta)\rangle$, respectively. A straight line would indicate a perfect match between the two statistics.

$$r(\theta) = f_2(\theta, \Omega_m, \Omega_\Lambda) \times \frac{\langle \mathcal{N}(\theta) M_{\rm ap}(\theta)\rangle}{\sqrt{\langle \mathcal{N}^2(\theta)\rangle \langle M_{\rm ap}^2(\theta)\rangle}}\,. \quad (16)$$

The functions f_1 and f_2 correct for the fact that different cosmological volumes are probed by the different statistics. They are defined as

$$f_1(\theta) = \sqrt{\frac{\langle M_{\rm ap}^2(\theta)\rangle}{\langle \mathcal{N}^2(\theta)\rangle}}\Bigg|_{r=b=1}\,, \quad (17)$$

$$f_2(\theta) = \frac{\sqrt{\langle \mathcal{N}^2(\theta)\rangle \langle M_{\rm ap}^2(\theta)\rangle}}{\langle \mathcal{N}(\theta) M_{\rm ap}(\theta)\rangle}\Bigg|_{r=b=1}\,, \quad (18)$$

and are computed assuming a Smith et al. (2003) nonlinear power spectrum with unbiased foreground galaxies ($b = r = 1$), an Eisenstein & Hu (1999) transfer function, and the WMAP7 cosmological parameters (Komatsu et al. 2011).

In Figure 2, we show the evolution of f_1 and f_2 as a function of scale and redshift. These functions are not constant in scale. The amplitude of the deviations is larger for the higher redshift samples of galaxies. In Figure 2, function f_1 for pair F1–B1 is nearly constant, whereas it varies by 25% for pair F5–B3. The scale dependence of f_1 and f_2 is due to the fact that many different physical scales are projected into the same angular bins, and the weighting functions in $\langle \mathcal{N}^2(\theta)\rangle$, $\langle M_{\rm ap}^2(\theta)\rangle$, and $\langle \mathcal{N}(\theta) M_{\rm ap}(\theta)\rangle$ are different.

Van Waerbeke (1998) showed that f_1 and f_2 do not depend on the shape of the power spectrum. We performed a set of tests to verify this statement and reached the same conclusion. We computed f_1 and f_2 with a power spectrum for the linear regime (Peacock & Dodds 1996) instead of a Smith et al. (2003) power spectrum. We altered the amplitude σ_8 and spectral index n_s by 20%, and we measured less than a 5% difference. The amplitude of the power spectrum does not have a strong influence on f_1 and f_2. Note, however, that the calibration functions f_1 and f_2 scale with Ω_m (Simon et al. 2007). We fixed it to the WMAP7 value.

3.3. Physical Scales

Because we make measurements in bins of angular separations rather than physical separation, the bias parameters we measure are averages of the true bias parameters $b(k, w)$ and $r(k, w)$ in k-space and comoving distances. Their respective expressions are given by (Hoekstra et al. 2002)

$$\langle b\rangle^2(\theta) = \frac{\int_0^{w_h} dw\, h_1(\theta, w) b^2(\frac{4.25}{\theta f_K(w)}, w)}{\int_0^{w_h} dw\, h_1(\theta, w)}\,, \quad (19)$$

$$\langle r\rangle(\theta) = \frac{\int_0^{w_h} dw\, h_3(\theta, w) r(\frac{4.25}{\theta f_K(w)}, w)}{\int_0^{w_h} dw\, h_3(\theta, w)}, \quad (20)$$

where the weighting functions $h_1(\theta, w)$ and $h_3(\theta, w)$ are, respectively,

$$h_1(\theta, w) = \left(\frac{p_f(w)}{f_K(w)}\right)^2 P_{\rm filter}(\theta, w)\,, \quad (21)$$

$$h_3(\theta, w) = \frac{p_f(w) g(w)}{[f_K(w)]^2} P_{\rm filter}(\theta, w)\,, \quad (22)$$

and the filtered matter power spectrum is

$$P_{\rm filter}(\theta, w) = 2\pi \int_0^\infty d\ell\, \ell\, P_m\left(\frac{\ell}{f_K(w)}, w\right)[I(\ell\theta)]\,. \quad (23)$$

Note that in Equations (19) and (20) the bias parameters $b(k, w)$ and $r(k, w)$ are estimated at scale $k = 4.25/\theta f_K(w)$. In these equations, it was assumed that the bias parameters are evolving slowly with scale and their product by the $I(x)$ filter was equivalent to the product by a Dirac $\delta_D(x)$ function. Note as well that the functions $p_f(z)$ and $p_f(z)g(z)$ are narrow in redshift space. As a result, very few angular scales are mixed together when bias parameters $b(k, w)$ and $r(k, w)$ are projected along the line of sight. Therefore, the shapes of the bias parameters $\langle b\rangle$ and $\langle r\rangle$ in real space and $b(k, w)$ and $r(k, w)$ in k-space are very similar.

We use the weighting functions h_1 and h_3 to relate the physical scales to the angular scales at which bias parameters are measured. The scales in physical units are obtained via the following expressions:

$$\langle R_b(\theta)\rangle = 2\pi \frac{\int_0^{w_h} dw\, h_1(\theta, w)}{\int_0^{w_h} dw\, h_1(\theta, w) \frac{4.25}{\theta f_K(w)}}, \quad (24)$$

$$\langle R_r(\theta)\rangle = 2\pi \frac{\int_0^{w_h} dw\, h_3(\theta, w)}{\int_0^{w_h} dw\, h_3(\theta, w) \frac{4.25}{\theta f_K(w)}}. \quad (25)$$

In Figure 3, we show the weighting functions h_1 and h_3 for our five different pairs of redshift bins. The bias we measure in the following is the averaged bias of the galaxies in the hatched regions. The h_1 and h_3 functions extend over the whole redshift range, but we only hatched the regions containing 68% of integrated signal in h_1 and h_3. We found the widths of the hatched regions to be SI.

4. SIMULATIONS

We use N-body simulations to quantify the effect of cosmic variance on our bias measurements. Theoretical estimates of the cosmic variance for mass aperture statistics exist (Schneider

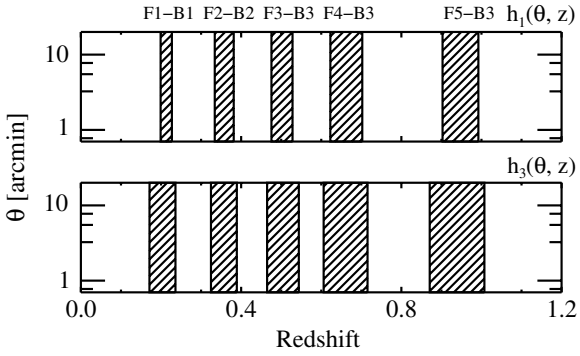

Figure 3. Five weighting functions $h_1(\theta, z)$ and $h_3(\theta, z)$ used to compute the analytical predictions of the bias parameters $\langle b \rangle$ and $\langle r \rangle$ for each bin F*i*–B*j*. In both panels, the five hatched areas contain 68% of the integrated signal in h_1 and h_3. The width of the hatched regions is scale independent.

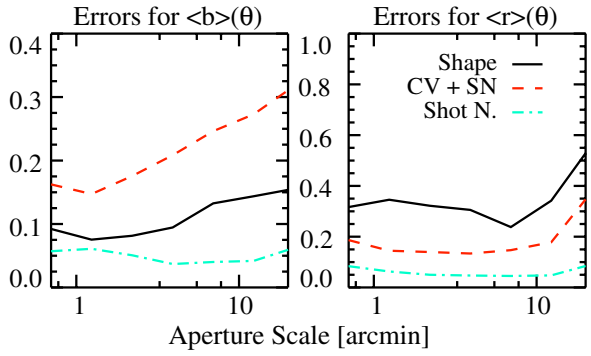

Figure 4. Error budgets for the galaxy bias parameters $\langle b \rangle(\theta)$ and $\langle r \rangle(\theta)$, obtained for foreground F1 and background B1. Shot noise and cosmic variance are obtained from simulations, whereas shape noise comes from the real data. (A color version of this figure is available in the online journal.)

et al. 2002; Joachimi et al. 2008), but they break down in the nonlinear regime, making simulations a necessity. These simulations will also help us to check our tools. Indeed, the mock galaxies in these simulations are pure dark matter particles and as such perfect tracers of the underlying dark matter. With our tools, we should therefore find $b = r = 1$ at all scales and all redshifts. Any deviation would highlight a flaw in our tools or an artifact in the method.

We generate a set of seven light cones of 10×10 deg^2 each, extending from redshift $z = 0$ to $z = 4$. The particle mass is $7.5 \times 10^{10}\, M_\odot$. We estimate the shear and convergence on a three-dimensional grid (fine in the angular direction, coarse in the radial direction), using a no-radial-binning method (Kiessling et al. 2011).

We make sure that the redshift distribution of the particles matches an Efstathiou et al. (1991) redshift distribution $p(z) \propto z^2 \exp[-(z/z_0)^2]$, with $z_0 = 0.78$ and 66 galaxies per square arcminute. This redshift distribution is close to the actual redshift distribution in COSMOS (Massey et al. 2007b). Finally, each simulated catalog is cut into 36 COSMOS-size catalogs, and we remove masked galaxies in the same way as we do with the real data. We obtain 343 mock catalogs of about 400,000 galaxies each. We bin these galaxies in redshift and randomly resample them so that the numbers of foreground and background galaxies match the numbers in Table 1. The redshift of the galaxies is computed analytically from their comoving distance assuming a WMAP7 cosmology. To keep it simple, we do not simulate photometric redshift uncertainties.

Figure 4 shows the error budget for the bias b and the correlation coefficient r computed for the foreground redshift bin F1 and the background bin B1. We split the error budget into cosmic variance, shot noise, and shape noise. To quantify the uncertainty in our results due to cosmic variance, we compute the bias parameters for each COSMOS realization. The variance of the resulting distribution is therefore due to cosmic variance and shot noise. To quantify the amount of shot noise only, we bootstrap the galaxies in one single COSMOS realization.

As shown in Figure 4, we find the cosmic variance for parameter $\langle b \rangle$ computed in foreground bin F1 and background bin B1 to be larger than the shape noise. In contrast for the correlation coefficient $\langle r \rangle$, shape noise dominates at all scales. $\langle r \rangle$ is more sensitive to shape noise because it contains the contributions from $\langle \mathcal{N}(\theta) M_{\rm ap}(\theta) \rangle$ and $\langle M_{\rm ap}^2(\theta) \rangle$, which are both affected by shape noise. We perform the same analysis with the other pairs in bins F*i*–B*j* and find that shape noise is always larger than cosmic variance for both bias parameters $\langle b \rangle$ and $\langle r \rangle$. The reason is that background galaxies in bins B2 and B3 are fainter, so their shape estimation is more noisy.

We also used the simulations to test our treatment of the photometric redshift, and especially the way we reconstruct the weighting functions $p_b(z)$ and $p_f(z)$ for the background and foreground redshift bins. We simulated photometric redshifts with different redshift uncertainties from $d_z/(1+z) = 0.01$ to $d_z/(1+z) = 0.05$. We reconstructed the weighting functions of bins F1 and B1. For bin F1 with $d_z/(1+z) = 0.05$, we measured the rms between the recovered and the true $p(z)$ to be rms $= 4.49 \pm 0.32$ for the standard histogram technique and rms $= 4.10 \pm 0.33$ for the sum of pdfs technique. For bin B1 with errors $d_z/(1+z) = 0.01$, we measured rms $= 0.48 \pm 0.01$ and rms $= 0.65 \pm 0.01$, respectively. Therefore, our technique is better for large redshift uncertainties and lower redshift bins. In our particular case, where redshift uncertainties are about $d_z/(1+z) = 0.05$ for the faint part of the samples, our technique is globally as good as constructing a standard histogram of the best-fit estimates. As already mentioned previously, we preferred this technique because galaxies outside the redshift limits were properly taken into account, which resulted in a better agreement between predicted and observed signals. To push this comparison further, more realistic galaxy redshift pdfs should be simulated, but this is out of the scope of this paper.

Note finally that our estimates of the systematic errors in our measurements of $\langle b \rangle$ and $\langle r \rangle$ might be underestimated because we do not consider scatter due to inaccurate photometric redshifts, and we do not populate the dark matter simulations with a realistic model of galaxies. Therefore, any additional scatter introduced by physical processes involved in galaxy formation will not be taken into account.

5. RESULTS

In this section, we present our measurements of the correlation functions. We use these measurements to derive the bias and estimate its scale and redshift dependence.

5.1. Correlation Functions

As described in Appendix A, aperture statistics are computed from auto- and cross-correlation functions. We use the software ATHENA,[7] which implements a tree code and computes auto- and cross-correlation functions. For the tree code, we

[7] http://www2.iap.fr/users/kilbinge/athena

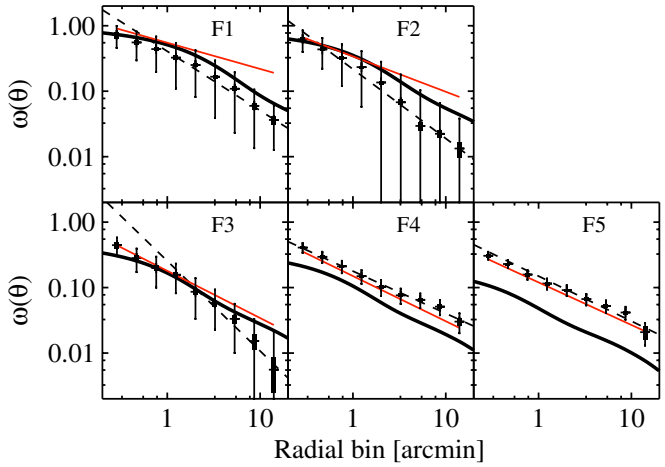

Figure 5. Projected galaxy autocorrelation for our flux-selected galaxy samples in bins F1 to F5. Dashed line: fit to the data with a power law. The best-fit scaling parameter A_w and slope δ are reported in Table 2; red line: power law with parameters inferred from the fit to $\langle\mathcal{N}^2(\theta)\rangle$. This represents the signal we should obtain after IC correction of $\omega(\theta)$ (see the text). Bold line: predicted signal derived from a Smith et al. (2003) power spectrum with unbiased galaxies. Error bars include shot noise (thick line) and cosmic variance (thin line). Cosmic variance always dominates the measurements.

(A color version of this figure is available in the online journal.)

choose an opening angle[8] of 0.04 rad. All correlation functions are measured in 950 logarithmic bins between 0.05 and 50 arcmin, which corresponds to a sampling scale of $\Delta\vartheta = 0.007\vartheta$. The aperture statistics and the bias parameters are also computed with this fine binning. We estimate the error bars with bootstrapping, i.e., we repeat the measurements 200 times with different galaxy samples randomly drawn from the input catalogs. For the figures, we rebin the data in coarse bins using a median binning technique. We used the median rather than the mean because the distributions of the bias parameters are not Gaussian, and so the median is more robust. However, this is a small correction since, with the mean instead, the bias parameters b and r would be only about 3% larger. To allow a straightforward comparison, we use the same binning for both the data and the simulations.

In the following, we will always compare our results to numerical predictions. We found the Smith et al. (2003) fitting formula to give a good approximation of the measurements at large scales. In contrast, at small scales, we found the fitting formula to underpredict the measurements (see, e.g., Figures 6, 8, and 9). Hilbert et al. (2009) had already noticed this discrepancy at scales $\ell > 10{,}000$ and suggested that it could be due to the low resolution of the simulations used by Smith et al. (2003). In our case, the discrepancies could at least partly also originate from the fact that we compare power spectra of biased galaxy samples and dark matter. Indeed, power spectra of galaxies are expected to deviate from pure dark matter power spectra. Analyzing these deviations as a function of scale, redshift, and galaxy properties is in fact the whole purpose of this paper. Therefore, comparing the measured and the predicted measurements already gives us a first guess by eye of the amplitude of galaxy bias for a particular galaxy population.

[8] In Athena, galaxy properties are spatially averaged in nodes. The opening angle between a central and a tangential node is the ratio between the size of the tangential node divided by the distance between the nodes. The properties of two nodes are correlated if the opening angle is smaller than 0.04 rad.

Table 2
Scaling and Slope of the Power-law Fit to $\omega(\theta)$

Bin	Direct Fit		IC Corrected Using $\langle\mathcal{N}^2(\theta)\rangle$	
	$A_w(1')$	δ	$A_w(1')$	δ
F1	0.32	0.75	0.61 ± 0.28	0.37 ± 0.12
F2	0.21	0.93	0.50 ± 0.16	0.41 ± 0.09
F3	0.15	0.93	0.22 ± 0.05	0.64 ± 0.08
F4	0.18	0.65	0.21 ± 0.03	0.54 ± 0.05
F5	0.14	0.63	0.15 ± 0.02	0.55 ± 0.03

Notes. The IC corrected amplitudes A_w and slopes δ are obtained from the fit to $\langle\mathcal{N}^2(\theta)\rangle$ and Equation (27).

Galaxy clustering. In Figure 5, we show the projected galaxy autocorrelation function $\omega(\theta)$ for our five foreground redshift bins. We compute $\omega(\theta)$ using the Landy & Szalay (1993) estimator defined as

$$\omega(\theta) = \frac{DD}{RR} - 2\frac{DR}{RR} + 1, \tag{26}$$

where the normalized numbers of pairs DD, RR, and DR refer to pairs of galaxy positions, random positions, and galaxy and random positions, respectively.

By bootstrapping the data, we include shot noise in the error bars for the data and cosmic variance for the simulations. At high redshift, we calculate smaller error bars because (1) high-redshift bins contain more galaxies and (2) we probe larger volumes and cosmic variance decreases in larger volumes. In bins F4 and F5, we observe 2σ and 3σ deviations, respectively, between the measured and the predicted signals. These deviations already suggest that our flux-selected galaxy samples are biased with respect to the matter distribution (see Equations (12) and (B1)).

Galaxy autocorrelation functions have been found to closely follow a power law (PL, e.g., McCracken et al. 2007). In order to assess the evolution of galaxy clustering with redshift, we fit a PL $\omega(\theta) = A_w(\theta/1')^{-\delta}$ to our measurements and report the best-fit parameters in Table 2. However, our estimator $\omega(\theta)$ is mathematically known only up to an additive constant known as the integral constraint (IC), which depends on the volume and the mean galaxy density of the sample (McCracken et al. 2007). In the next section, we present how we correct for IC using the $\langle\mathcal{N}^2(\theta)\rangle$ measurements.

Galaxy–galaxy lensing. In Figure 6, we show the evolution with redshift of the galaxy–galaxy lensing measurements for our five flux-selected galaxy samples. Overall, we observe our measurements to decrease with scale. To correct for systematic effects at large scales, we subtracted the signal measured around random foreground galaxies (Mandelbaum et al. 2005). To guide the eye, we overplot the predicted signal derived from the Smith et al. (2003) power spectrum with unbiased galaxies. The match is good at large scales, but we note a discrepancy at small scales. To assess the significance of this discrepancy, we compared the slopes of the data and the predictions at scales $\theta < 3'$. Taking into account the correlation between the data points, we fitted five PL functions to the data at these scales and found their slopes to be always negative at 2σ confidence level, hence at odds with the positive slopes of the predictions. This highlights the limited accuracy of the Smith et al. (2003) power spectrum at small scales.

Shear autocorrelation. Finally, we compute the shear autocorrelation functions ξ_+ and ξ_- for our three background catalogs

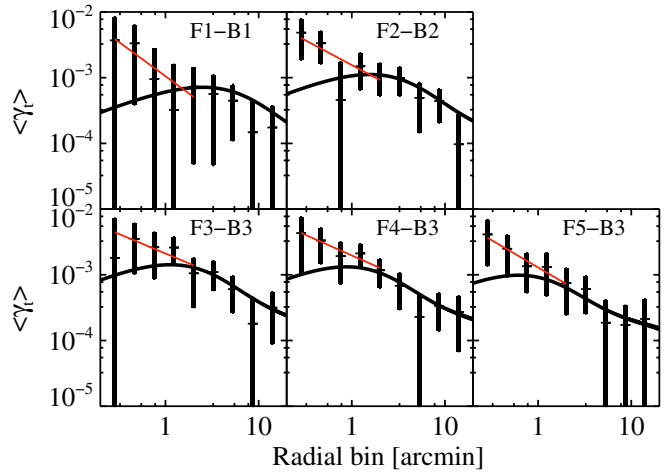

Figure 6. Mean tangential shear as a function of scale and redshift. The signal measured around random foreground galaxies has been subtracted to correct for systematic errors. To guide the eye, we overplot predictions derived from the Smith et al. (2003) power spectrum with unbiased galaxies (solid line). We fitted power-law functions to the data at small scales (red lines) to assess the significance of the discrepancy with the predictions. Error bars include shape noise and shot noise (thick line), and cosmic variance (thin line).

(A color version of this figure is available in the online journal.)

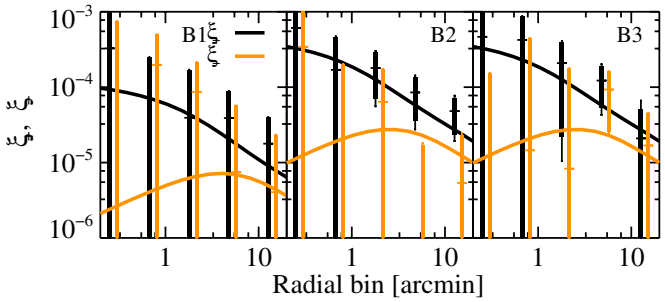

Figure 7. Shear–shear correlation function for the three background source catalogs B1–B3. Solid lines are the predicted signal with a Smith et al. (2003) power spectrum. Error bars include shape noise and shot noise (thick line), and cosmic variance (thin line).

(A color version of this figure is available in the online journal.)

B1, B2, and B3. They are presented in Figure 7. The amplitude increases between B1 and B3 mainly because the lensing efficiency in Equation (13) increases with redshift. The contribution of the structures along the line of sight is likely small, because they are mostly uncorrelated.

5.2. Aperture Statistics

In this section, we derive aperture statistics from the correlation functions. The calculations are detailed in Appendix A.

Galaxy aperture variance. The measurements of $\langle\mathcal{N}^2(\theta)\rangle$ for the five foreground bins are shown in Figure 8. For each redshift bin, we fit a PL. In contrast to $\omega(\theta)$, $\langle\mathcal{N}^2(\theta)\rangle$ is not affected by IC, because the compensated filter T_+ that multiplies $\omega(\theta)$ in Equation (A10) cancels out any constant, including IC (Schneider et al. 1998). Simon et al. (2007) derived an analytic relation between the parameters of a PL fit to $\langle\mathcal{N}^2(\theta)\rangle$ and the parameters of a PL fit to an IC corrected correlation function $\omega(\theta)$. The slope of $\omega(\theta)$ corrected for IC is given by

$$f(\delta) = 0.0051\delta^{11.55} + 0.2769\delta^{3.95} + 0.2838\delta^{1.25}, \qquad (27)$$

where δ is the slope of the PL fit to $\langle\mathcal{N}^2(\theta)\rangle$. The amplitude of the PL fit to $\omega(\theta)$ is the same as the amplitude of the PL fit

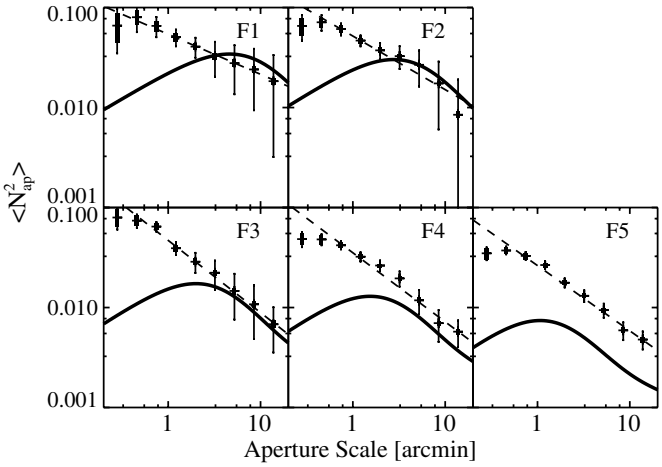

Figure 8. Galaxy aperture variance. To guide the eye, we overplot the predicted signal derived from a Smith et al. (2003) power spectrum with unbiased galaxies (solid line). As expected, the prediction underestimates the signal at small scales. At large scales, the deviation in bins F4 and F5 already suggests that galaxies are biased (see also Figure 11). Error bars include shot noise (thick line) and cosmic variance (thin line).

to $\langle\mathcal{N}^2(\theta)\rangle$. In Table 2, we report the IC-corrected amplitudes A_w and slopes δ of the galaxy autocorrelation function $\omega(\theta)$ obtained from Equation (27).

We find that the amplitude A_w decreases with redshift, in agreement with McCracken et al. (2007), who also found smaller amplitudes for fainter galaxies in COSMOS, i.e., more likely located at higher redshift. Besides, we note a jump in amplitude between bins F3 and F2, i.e., between redshift $z \sim 0.52$ and $z \sim 0.35$. With respect to the slope δ, we observe a slight but not significant (less than 1σ) steepening with redshift. Such a peculiar behavior could be explained by the large-scale structure identified at redshift $z \sim 0.7$ already detected in several other studies (Massey et al. 2007a; Guzzo et al. 2007; Meneux et al. 2009; de la Torre et al. 2010). We guess that more massive galaxies in this structure would increase the slope because they are typically more clustered than average.

Finally, we observe an increasing deviation (more than 5σ in bin F5) between the measurements and the signal predicted with a Smith et al. (2003) power spectrum and unbiased galaxies. This suggests that galaxies are more biased at high redshift, in agreement with expectations. For bin F4 in the last three bins, we find on average a bias of about 1.4 between the data and the predictions, and for bin F5 in the last five bins, we find a bias of about 2.6.

Galaxy-mass aperture covariance. The measurements of $\langle\mathcal{N}(\theta)M_{\rm ap}(\theta)\rangle$ for our five foreground redshift bins are shown in Figure 9. In agreement with the $\langle\gamma_t\rangle$ measurements, we again note that a Smith et al. (2003) power spectrum underpredicts the data points at small scales. We performed a χ^2-test and found this disagreement to be significant in all bins at more than 3σ (we included the covariance matrices in the χ^2-test). This disagreement is also present for the stellar-mass-selected galaxy samples in Figures 16 and 17. At small scales in bins F2–B2, we also note a slight change of slope at $1'$ scale. Again, we investigated the significance of this feature with a χ^2-test but found a reduced $\chi^2 = 1.60$, which is not enough to reject a simple PL model.

An E/B mode decomposition also exists for the $\langle\mathcal{N}(\theta)M_{\rm ap}(\theta)\rangle$ statistics. $\langle NM_{\rm x}\rangle$ quantifies the amount of B-modes in the measurement and is computed by replacing

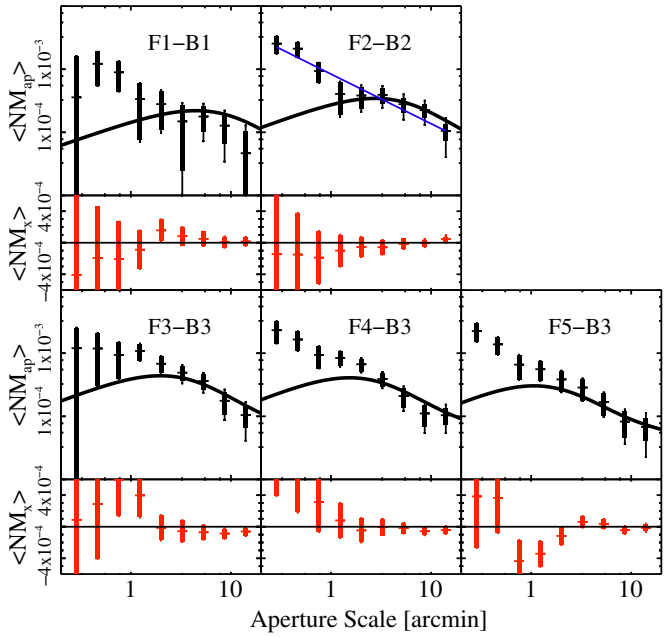

Figure 9. Galaxy-mass aperture covariance as a function of scale and redshift. To guide the eye at large scale, we also show the predictions derived from the Smith et al. (2003) power spectrum with unbiased galaxies (solid line). For bins F2–B2, we found the change of slope to be not significant compared to a power-law fit (blue line). In red, $\langle NM_{\rm x}\rangle$ quantifies the amount of "B-modes" (see the text). Error bars include shape noise (thick line) and cosmic variance (thin line).

(A color version of this figure is available in the online journal.)

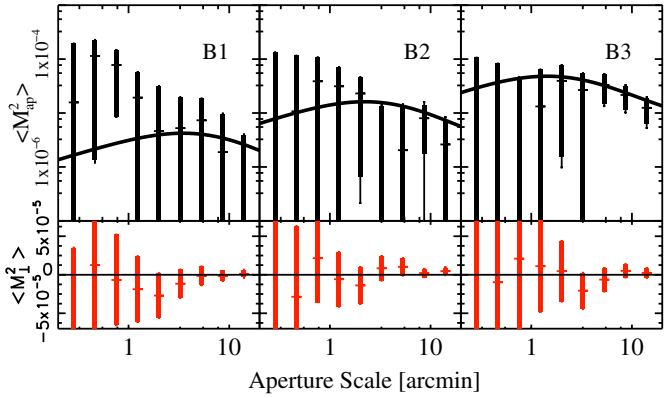

Figure 10. Mass-aperture variance as a function of scale and redshift. To guide the eye, we overplot predictions derived from the Smith et al. (2003) power spectrum. In bins F2–B2, we fitted a power law (blue line) to the data and found the change of slope to be not significant. In red: the "B-modes" are consistent with zero at all scales in all bins. Errors include shape noise and shot noise (thick line), and cosmic variance (thin line).

(A color version of this figure is available in the online journal.)

γ_t by γ_x in Equation (A11). γ_x is the galaxy–galaxy clustering signal obtained with the coordinate system rotated by 45°. This operation is commonly used to reveal B-mode contamination if an $\langle NM_{\rm x}\rangle$ signal is detected. Using a χ^2-test and taking into account the correlation between the data points, we find the B-modes for $\langle NM_{\rm x}\rangle$ to be consistent with zero in all bins F*i*–B*j* at 95% confidence level, hence confirming a very low level of contamination in our analysis.

Mass aperture variance. The measurements of $\langle M^2_{\rm ap}(\theta)\rangle$ for bins B1, B2, and B3 are shown in Figure 10. The solid line represents the predicted signal with a Smith et al. (2003) power

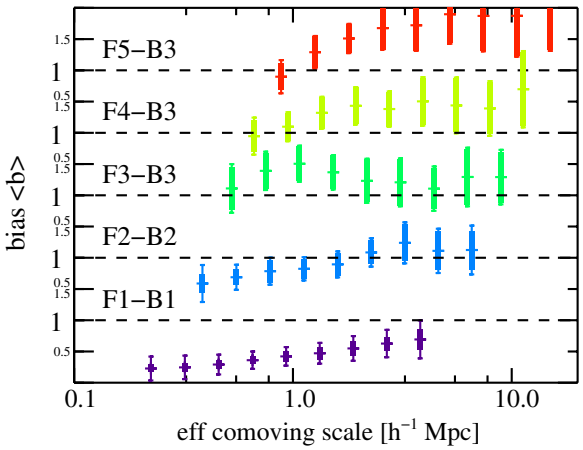

Figure 11. Evolution of bias in comoving scale and redshift for the flux-limited galaxy sample. Bias increases with redshift both because flux-selected galaxies reside in more massive halos and because halos of any given mass are more biased at high redshift. At small scales, the change of slope can be interpreted as the transition between the two-halo and the one-halo terms in a halo model framework. Error bars include shape and shot noise (thick line), and cosmic variance (thin line). The horizontal dashed line marks the value $b = 1$ for each bin. The data points are correlated (see Section 5.6).

(A color version of this figure is available in the online journal.)

spectrum. We performed a χ^2-test between the data points and the predicted signal and found that the data points are consistent with the predicted signal at 68% confidence level for all bins B1, B2, and B3. At all scales, shape noise dominates over cosmic variance. Errors are smaller for bin B3, because the signal is larger (about 10 times larger than the signal in bin B1).

5.3. Bias of the Flux-selected Sample

5.3.1. Constant Bias Model

In Figure 11, we show the galaxy bias $\langle b\rangle(R)$ for our sample of flux-limited galaxies. We observe that bias varies with scale and redshift, but since the data points are correlated, we use a χ^2-test to quantify the significance of these variations. First, we assume the null hypothesis that bias is scale and redshift independent. To test this hypothesis, we fit a constant b_0 to the 45 data points in the five redshift bins and compute the χ^2 statistics

$$\chi^2 = (\mathbf{B} - b_0)^T C^{-1} (\mathbf{B} - b_0), \tag{28}$$

where $\mathbf{B}$ is a vector containing the 45 data points and C is their covariance matrix. To perform the fit and find the best-fit parameters, we use the IDL AMOEBA technique (Nelder & Mead 1965) and repeat the process 100 times with different starting values. We obtain a best fit with $\chi^2 = 229$. Our data points are correlated, so the effective number of degrees of freedom (dof) to perform the χ^2 test is less than the number of data points $N = 45$ minus the number of free parameters. Bretherton et al. (1999) proposed several estimators for the number of dof for correlated data. We use the estimator[9]

$$\mathrm{dof} = \frac{N^2}{\sum_{ij} r_{ij}^2}, \tag{29}$$

where r_{ij} is the correlation coefficient between data points b_i and b_j, and N is the number of data points. Using this estimator, we

[9] Bretherton et al. (1999) mainly studied another estimator $\mathrm{dof} = (\sum_i C_{ii})^2 / \sum_{ij} C_{ij}^2$, which is equivalent if the data points are centered and normally distributed with unit variance.

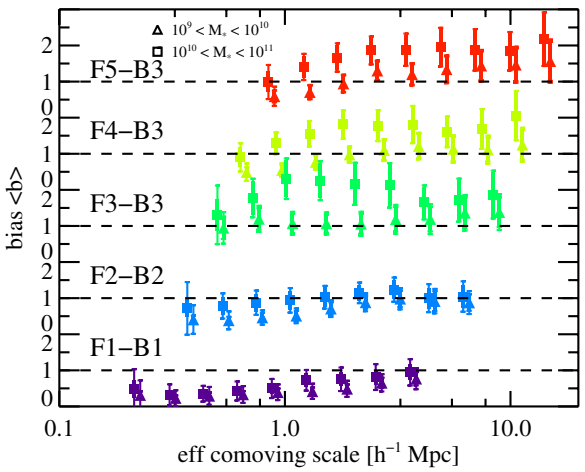

Figure 12. Same as Figure 11, but for stellar-mass-selected galaxies. Bias increases with redshift and stellar mass. The horizontal dashed line marks the value $b = 1$ for each bin.

(A color version of this figure is available in the online journal.)

find dof $= 32-1 = 31$, where we subtracted 1 for the parameter we fit. The reduced χ^2 is therefore $\chi^2/\mathrm{dof} = 7.4$, which allows us to confidently reject a constant bias model given our data.

5.3.2. Redshift-dependent Model

Here, we discuss a test of the redshift dependence of bias. To our model, we add the following redshift dependence:

$$b(z) = b_0 + b_1 z\,. \tag{30}$$

We obtain a reduced $\chi^2/\mathrm{dof} = 2.5$. Although still not a good fit, this model is nonetheless significantly better than the previous redshift-independent model.

So far, we have ruled out a constant bias with redshift and scale, but we did not isolate the redshift dependence or scale dependence yet. This is the purpose of the rest of this section.

5.3.3. Scale-independent Model

Next, we test the scale dependence only. Our null hypothesis is now that bias is SI. For each redshift bin, we fit a constant and sum the χ^2 for each individual redshift bin. We obtain a total $\chi^2 = 43$ for an effective number of degrees of freedom dof $= 32 - 5 = 27$. This means that there is a 97.4% chance that the SI model is wrong. Here, we subtracted 5 for the five constant parameters we fit. A fit of this model to the stellar-mass-selected galaxy samples brings less stringent constraints, with $\chi^2/\mathrm{dof} = 1.49$ and $\chi^2/\mathrm{dof} = 1.0$ for the low and high stellar-mass-selected samples, respectively.

5.4. Bias of the Stellar-mass-selected Sample

In Figure 12, we show the galaxy bias $\langle b\rangle$ for two stellar-mass-selected galaxy samples as a function of scale and redshift. Previous studies have shown that stellar mass is a good tracer of halo mass (see, e.g., Leauthaud et al. 2012, and references therein), which in turn parameterizes most of the bias models. In contrast, flux-selected samples are more affected by selection effects. For instance, low surface brightness extended galaxies are systematically underrepresented because they tend to evade the magnitude cuts (Meneux et al. 2009). Our stellar-mass-selected samples should therefore tell us more about halo properties.

5.4.1. Halo Mass

First, we derive the average halo mass for our two samples of galaxies. For this purpose, we fit the bias model proposed by Tinker et al. (2010)

$$b(\nu) = 1 - A\frac{\nu^a}{\nu^a + \delta_c^a} + B\nu^b + C\nu^c, \tag{31}$$

defined in terms of the peak height $\nu = \delta_c(z)/D(z)\sigma(M)$, where $\delta_c(z)$ is the critical density for halo collapse (Weinberg & Kamionkowski 2003), $D(z)$ is the growth factor, and $\sigma^2(M)$ is the variance of the density fluctuations smoothed with a top-hat filter of size $R = (3M/4\pi\bar{\rho}_m)^{1/3}$. The parameters of this fitting function derive from fits to N-body simulations. They are $A = 1.0 + 0.24y\exp(-(4/y)^4)$, $a = 0.44y - 0.88$, $B = 0.183$, $b = 1.5$, $C = 0.019 + 0.107y + 0.19\exp(-(4/y)^4)$, and $c = 2.4$. We define the parameter $y \equiv \log_{10}\Delta$ for overdensity $\Delta = 200$ times the cosmological mean density.

Although this bias model is not explicitly a redshift-dependent model, we make use of the fact that ν scales with redshift to test the redshift dependence of our measurements.

The Tinker et al. (2010) model is a halo bias model, i.e., it was calibrated on halo clustering measured in N-body simulations. In contrast, we measure galaxy clustering for stellar-mass-selected galaxies. Using it to infer halo mass implies the two following assumptions: (1) the dark matter mass function is constant in the range of halo mass we consider, and (2) there is only one galaxy per halo. The first assumption is valid because our galaxies are embedded in halos with peak height $\nu \sim 1$ and mass $\log_{10}(M/M_\odot) \leqslant 13$, and the halo mass function in this regime is almost flat (Sheth & Tormen 1999; Tinker et al. 2008). The second assumption holds in the linear regime where most of the signal comes from the clustering of central galaxies.

To overcome the problem of having data points at different redshifts, we fit a redshift-normalized peak height parameter ν_0, defined such that $b(\nu_i) = b(\nu_0/D(z_i))$, where z_i is the redshift of a data point b_i. Since this model is only valid in the linear regime, we only consider the 16 data points at scales $R > 2\,h^{-1}$ Mpc. We find $\chi^2 = 3.13$ and $\chi^2 = 4.93$ for dof $= 10.8$ and dof $= 11.2$, respectively, for the low and high stellar-mass galaxy samples. Therefore, the model proposed by Tinker et al. (2010) fits well our data.

This implies that our measurements agree with an increase of bias with redshift. In addition, we can derive the halo mass of our two stellar-mass-selected galaxy samples. Indeed, the best-fit values are $\nu_0 = 0.77^{+0.20}_{-0.31}$ and $\nu_0 = 1.01^{+0.24}_{-0.18}$ for the low and the high stellar-mass samples, respectively. To compare to Leauthaud et al. (2012), we compute the peak height estimator at redshift $z = 0.37$, $\nu_{z=0.37} = \nu_0/D(0.37) = 0.93$ and 1.21 for the low and high stellar-mass samples, respectively. This translates into $9.64 < \log_{10}(M_{200}/h^{-1}\,M_\odot) < 12.29$ and $11.51 < \log_{10}(M_{200}/h^{-1}\,M_\odot) < 12.80$, respectively. These results are in very good agreement with Leauthaud et al. (2012), when considering that our two stellar-mass-selected samples range between $10^9\,h^{-2}\,M_\odot < M_* < 10^{10}\,h^{-2}\,M_\odot$ and $10^{10}\,h^{-1}\,M_\odot < M_* < 10^{11}\,h^{-2}\,M_\odot$. As a last check, we also fit the Sheth et al. (2001) bias model and found similar results. The data are not stringent enough to distinguish the two models.

In Figure 13, we show the evolution of bias with redshift. The data points are averages of points at scales $R > 2\,h^{-1}$ Mpc, and errors come from the respective total covariance matrices. The total covariance matrix is the sum of the data covariance matrix and the simulation covariance matrix. The shape noise,

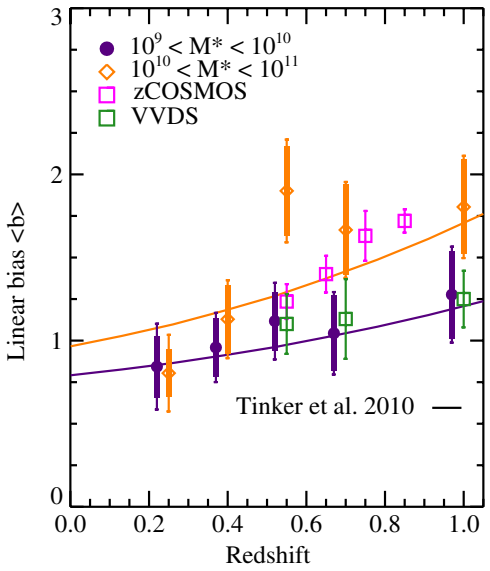

Figure 13. Redshift evolution of bias averaged on scales $R > 2\,h^{-1}$ Mpc for the two stellar-mass-selected galaxy samples. Error bars include shape noise, shot noise (thick line), and cosmic variance (thin line). Solid lines are the best fit predicted by the Tinker et al. (2010) halo bias fitting function. At $z = 0.37$, the halo masses predicted by the model are $\log(M_{200}/h^{-1}\,M_\odot) = 11.58$ and $\log(M_{200}/h^{-1}\,M_\odot) = 12.36$ for the low and high stellar-mass-selected galaxy samples, respectively. Green boxes are measurements in VVDS for a volume-limited ($\mathcal{M}_B < -20 + 5\log h$) galaxy sample (Marinoni et al. 2005). Pink boxes are measurements in zCOSMOS for $M_B < -20 - z$ galaxies (Kovač et al. 2011).

(A color version of this figure is available in the online journal.)

shot noise, and cosmic variance are thus taken into account. For comparison, we overplot the bias measured by Kovač et al. (2011) with the zCOSMOS data set and by Marinoni et al. (2005) (M05) with the VLT VIMOS Deep Survey (VVDS). The zCOSMOS data set is the same as ours but with galaxies brighter than $I_{814} < 22.5$. The bias measured by Kovač et al. (2011) follows our high stellar-mass galaxy samples, whereas the bias measured by M05 follows our low-mass samples. We attribute the difference in bias between the two measurements to differences in galaxy selection functions.

We found bias in bins F3–B3 for the high stellar-mass galaxy sample to be larger than expected. Although this data point still agrees with the bias model predictions at 95% confidence level, it shall be discussed further. Indeed at a similar redshift, Kovač et al. (2011) also identified a significant overdensity of galaxies that could explain the large bias value, but Finoguenov et al. (2007) identified very few massive groups. These two inconsistent observations are puzzling. A halo model like the one proposed by Leauthaud et al. (2011) could help us understand better the peculiar properties of the galaxies at this redshift, in particular the fraction of satellite galaxies.

5.4.2. Scale-dependent Model

In Section 5.3, we showed that an SD bias model was preferred but still not significantly better than an SI model. Nonetheless, we observe by eye that bias systematically decreases at small scales, and the turndown seems to start at scale $R \sim 2\,h^{-1}$ Mpc, which could correspond to the transition between the one-halo and the two-halo term, already identified in several previous papers. According to Zehavi et al. (2005), the behavior of bias at this transition scale is due to pairs of satellite galaxies. With a halo model applied to simulated data, Kravtsov et al. (2004) showed that a significant amount of pairs with satellite galaxies was crucial for a smooth transition. Coupon et al. (2011), using the CFHT Legacy Survey, and Peng et al. (2011), with SDSS data, also found that the fraction of satellite galaxies depends more on their local over-density than on the halo mass or redshift. Since overdensities increase at late time, the number of satellite galaxies increases in low-redshift samples of galaxies. A change of slope in our data would therefore indicate a change of the satellite fraction in the galaxy samples.

Table 3
Best-fit Parameters for the Scale and Redshift-dependent Model (Equation (32)) Applied to the $10^9\,h^{-2}\,M_\odot < M^* < 10^{10}\,h^{-2}\,M_\odot$ (Low) and $10^{10}\,h^{-2}\,M_\odot < M^* < 10^{11}\,h^{-2}\,M_\odot$ (High) Stellar-mass-selected Samples

	Low	High
$R_{\rm TD}\,h^{-1}$ Mpc	2.6 ± 1.2	$1.0^{+0.8}_{-0.2}$
α_1	$0.42^{+0.32}_{-0.21}$	0.63 ± 0.18
α_2	$-0.17^{+0.44}_{-0.41}$	-0.44 ± 0.24
$\log M_{200}/h^{-1}\,M_\odot$	$11.7^{+0.6}_{-1.3}$	$12.4^{+0.2}_{-2.9}$
χ^2/dof	0.7	1.0

In order to measure the significance of an evolution of the slope with redshift, we parameterize it as $\alpha(z) = \alpha_1 + \alpha_2 z$. We also introduce a turn-down scale $R_{\rm TD}$ beyond which bias evolves linearly. The final SD bias model we fit to the data is

$$b(R, z) = b_{\rm lin}(\nu) \begin{cases} \left(\dfrac{R}{R_{\rm TD}}\right)^{\alpha_1+\alpha_2 z} & R < R_{\rm TD} \\ 1 & R \geqslant R_{\rm TD} \end{cases}, \qquad (32)$$

where we use the redshift-dependent bias model $b_{\rm lin}(\nu)$ of Tinker et al. (2010) to describe the bias in the linear regime. We find $\chi^2/{\rm dof} = 0.7$ and $\chi^2/{\rm dof} = 1.0$ for the low and high stellar-mass-selected samples, respectively. The best-fit parameters are reported in Table 3.

The difference in χ^2 between the SI and SD models $\Delta\chi^2 = \chi^2_{\rm SI}/{\rm dof}_{\rm SI} - \chi^2_{\rm SD}/{\rm dof}_{\rm SD} = 0.79$ is not large enough to completely rule out the SI bias model.

The best-fit parameters of the SD model merit some particular attention. First, the scale at which bias turns down is detected to be between $0.8\,h^{-1}$ Mpc and $3.8\,h^{-1}$ Mpc at 68% CL. In contrast to what was observed in SDSS (Johnston et al. 2007), the data suggest $R_{\rm TD}$ to be marginally larger for less massive galaxies, but we would need more bins in stellar mass to confirm this tendency.

Second, the slope of bias at scales below $R_{\rm TD}$ is detected to be larger than zero, but at less than 2σ CL. We measured $\alpha_1 = 0.42^{+0.32}_{-0.21}$ and $\alpha_1 = 0.63 \pm 0.18$ for the low and high stellar-mass samples, respectively. Regarding its evolution with redshift, we found $\alpha_2 = -017^{+0.44}_{-0.41}$ for the low stellar-mass galaxy sample, hence no significant evolution, but $\alpha_2 = -0.44 \pm 0.24$ for the high stellar-mass-selected sample, hence a slight flattening of the slope at small scales at higher redshift bins.

It is expected that the steepness of the slope is related to the occurrence of satellite galaxies in our sample, with more satellite galaxies producing shallower slopes. The coincident fact that the turn-down scale is larger and the slope is shallower for the low stellar-mass sample suggests a larger amount of satellite galaxies in our low stellar-mass-selected sample.

5.5. Correlation Coefficients

In Figure 14, we show the correlation coefficient $\langle r \rangle$ for our flux-limited galaxy samples. Our measurements agree with

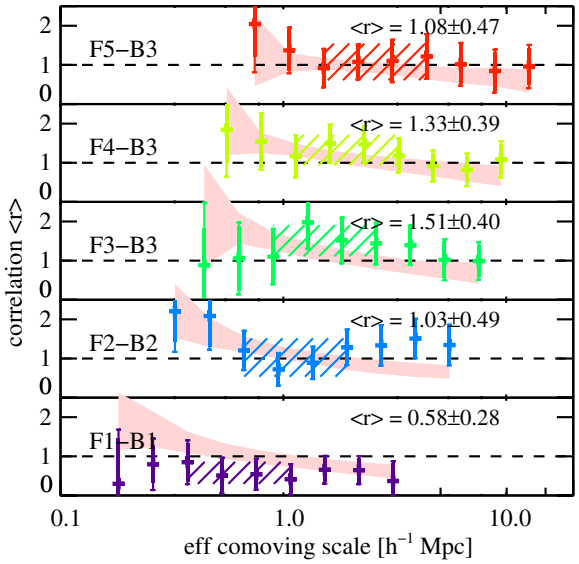

Figure 14. Correlation coeffcient $\langle r \rangle$ measured in redshift bins for our flux-limited galaxy samples. A deviation from $r = 1$ suggests that the bias relation is stochastic and not perfectly linear. Our method produces artificial deviations from $r = 1$, which we quantify with pure dark matter simulations (pink area) for which we know a priori that $r = 1$. The size of the pink area is due to cosmic variance. The hatched area individuates the range of scales where the simulations are consistent with $r = 1$. The averaged values of r are computed in these areas.

(A color version of this figure is available in the online journal.)

$r = 1$ at all scales and all redshifts. We nonetheless observe some trend in the data that might arise from possible artifacts in the method (see Section 6). To highlight them, we applied the method to the simulated data and indeed found a trend with a signal greater than 1 at small scale and lower than 1 at large scale. We show the correlation coefficient and errors obtained from the simulations as pink regions. Consequently, the trends we observe in our data points can be explained by artifacts in the method. The pink hatched regions mark the scales where r is consistent with 1 in the simulations. To compute the correlation factor for a particular galaxy sample, we only average the data points in these regions.

We found no significant deviation from $r = 1$, although in bins F1–B1, we obtain $r = 0.58 \pm 0.28$. Hoekstra et al. (2001) and Simon et al. (2007) found the correlation coefficient $\langle r \rangle < 1$ at 8σ, highlighting some stochasticity in the bias relations of their galaxy samples. In our case, we can only say that our flux-selected and stellar-mass-selected samples are good tracers of the underlying mass distribution given the error bars (see also Figures 16 and 17 for the results with the stellar-mass samples).

We have found no standard halo model to predict the scale dependence of the correlation coefficient r. In contrast, Neyrinck et al. (2005) propose a galaxy–halo model that does. In their model, they assume that halos attach to galaxies, in contrast to the standard halo model where galaxies attach to halos. By construction, assuming that all halos have the same density profile, the correlation coefficient is always $r = 1$. In the case in which halos have different density profiles, the correlation factor becomes SD. At large scales, many halos are averaged over, resulting in a mean density profile. The matter distribution therefore matches the galaxy distribution and $r = 1$. At scales smaller than the minimum intergalactic distance, r drops below 1 because of the many different density profiles. Finally, assuming that the inner parts of the density profiles are similar, r raises back to 1.

In light of this model, we attempt to identify a dip in bins F1–B1 and F2–B2 at scale $R \sim 2\,h^{-1}$ Mpc. Hoekstra et al. (2002) and Simon et al. (2007) also obtained such a dip at scale $R \sim 1\,h^{-1}$ Mpc with much higher significance. We fit a constant $r = 1$ to our data points in the hatched areas and measured $\chi^2 = 3.45$ in bins F1–B1 (dof = 2.75, >68% CL at $\chi^2 > 3.20$) and $\chi^2 = 2.20$ in bins F2–B2 (dof = 3.06, >68% CL at $\chi^2 > 3.57$). A constant model $r = 1$ therefore still provides a good fit to the data.

5.6. Bias Correlation Matrix

Figure 15 shows the correlation matrix of the bias (including cosmic variance) for the flux-limited galaxy sample F1–B1. The data points are significantly correlated between $1'$ and $10'$ for the bias parameter $\langle b \rangle$ and less correlated for the correlation coefficient. The large amount of correlation at the smallest scales $\theta < 0.'4$ is due to numerical artifacts (see Section 6).

Note as well that the large correlation between the angular bins for parameter $\langle b \rangle$ only shows up when the covariance matrix derived from simulations is added to the covariance matrix derived from the data. Otherwise, the amount of correlation is weak because of the low signal to noise in the data. The signal to noise in the simulated data is much higher, hence the stronger signal in the correlation matrix.

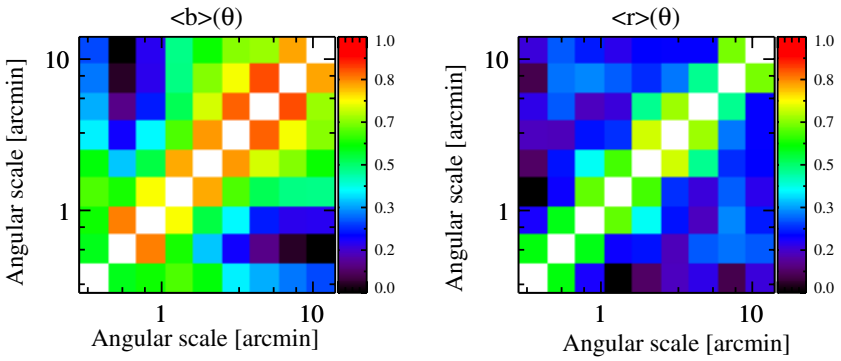

Figure 15. Left: the correlation matrix of estimator $\langle b \rangle(\theta)$ for data points in Figure 11 in bins F1–B1. Right: the correlation matrix of estimator $\langle r \rangle(\theta)$ in Figure 14 in bins F1–B1. Both correlation matrices include shape noise, shot noise, and cosmic variance.

(A color version of this figure is available in the online journal.)

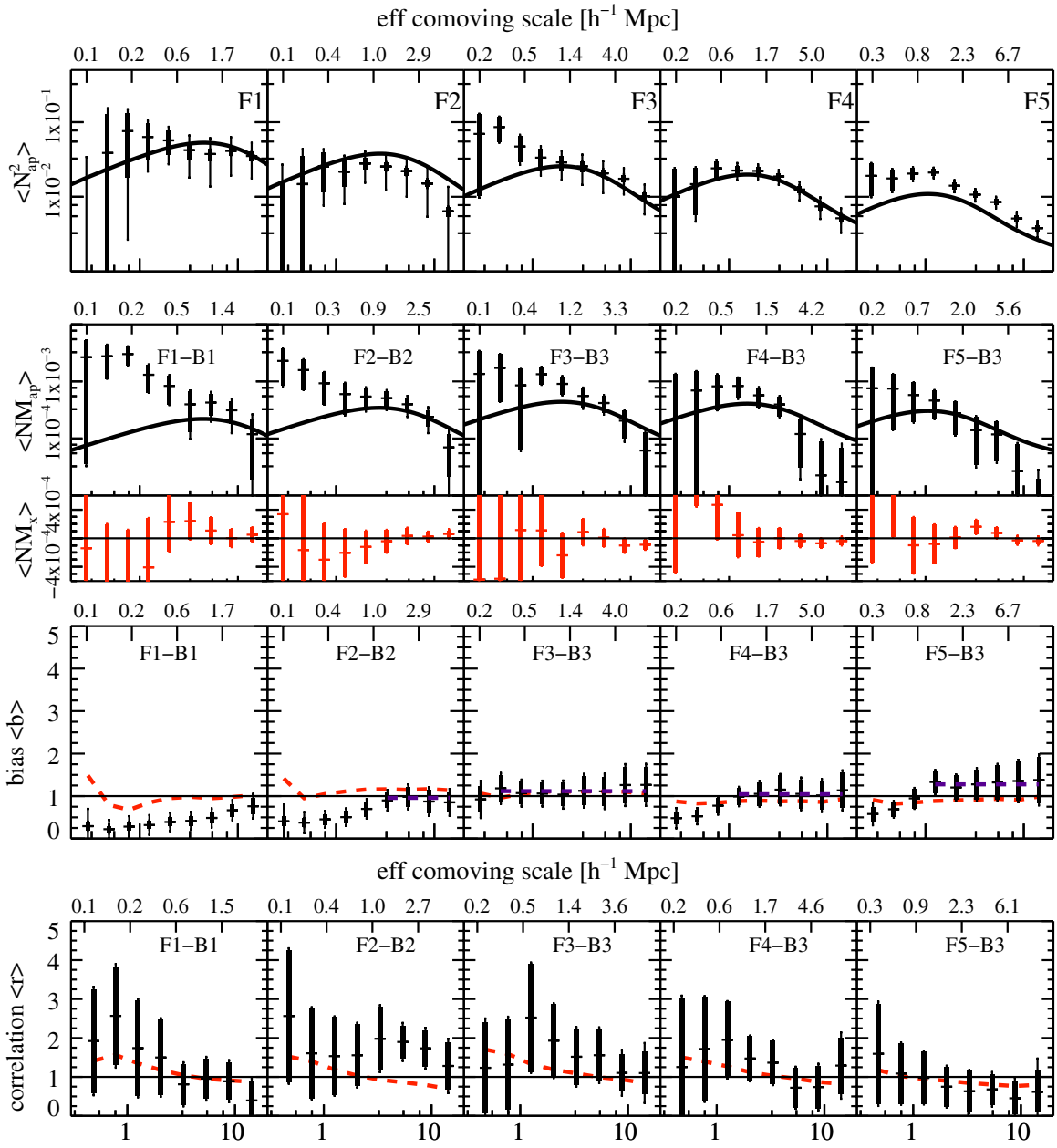

Figure 16. Overview of the most important estimators involved in the measurement of bias and stochasticity for the stellar-mass-selected galaxy sample in the range $10^9 < M_* < 10^{10}\,h^{-2}\,M_\odot$. The black curve in the two upper panels is the theoretical prediction derived from a Smith et al. (2003) power spectrum, and it is meant to guide the eye at large scales. The discrepancies at small scales are expected (see the text). The red dashed curves are the signals obtained in the simulations, which highlight numerical artifacts. Data points must be interpreted with respect to these curves rather than $b = 1$ and $r = 1$.

(A color version of this figure is available in the online journal.)

6. DISCUSSION

6.1. Artifacts in the Measurements

It is well known that aperture statistics, obtained through integration of other estimators, are very sensitive to integration limits. Kilbinger et al. (2006) found that the signal is underestimated by more than 10% at 12 times the lower integration limit, i.e., 0.′6 in our case. On the other hand, at large scales, the signal is only valid up to half the upper scale limit (see Equations (9) and (8)). We used simulations to assess the systematic effects produced by aperture statistics. In Figure 16 and 17, our simulations show that the correlation coefficient $\langle r \rangle$ is overestimated by 10% to 50% at scales $\theta < 1'$, depending on the redshift bin. For the bias parameter $\langle b \rangle$, deviations from $b = 1$ occur at scales $\theta < 0.'7$.

In the simulations, we also observed that the cross-correlation signals $\langle \mathcal{N}(\theta) M_{\rm ap}(\theta) \rangle$ and $\langle \gamma_t \rangle$ are biased low at large scales. Subtracting the signal measured around random foreground did not help in recovering $r = 1$ at large scales. We found this effect to be less important as the number of foreground galaxies decreases with respect to the number of background galaxies. This can be seen by comparing the red dashed lines in Figures 16 and 17. Although this effect is of minor consequence on our measurements given the size of the error bars, we tried to understand it. It is possible to demonstrate analytically that a constant additive systematic will cancel between sources 90° separated. When foreground galaxies do not have sources

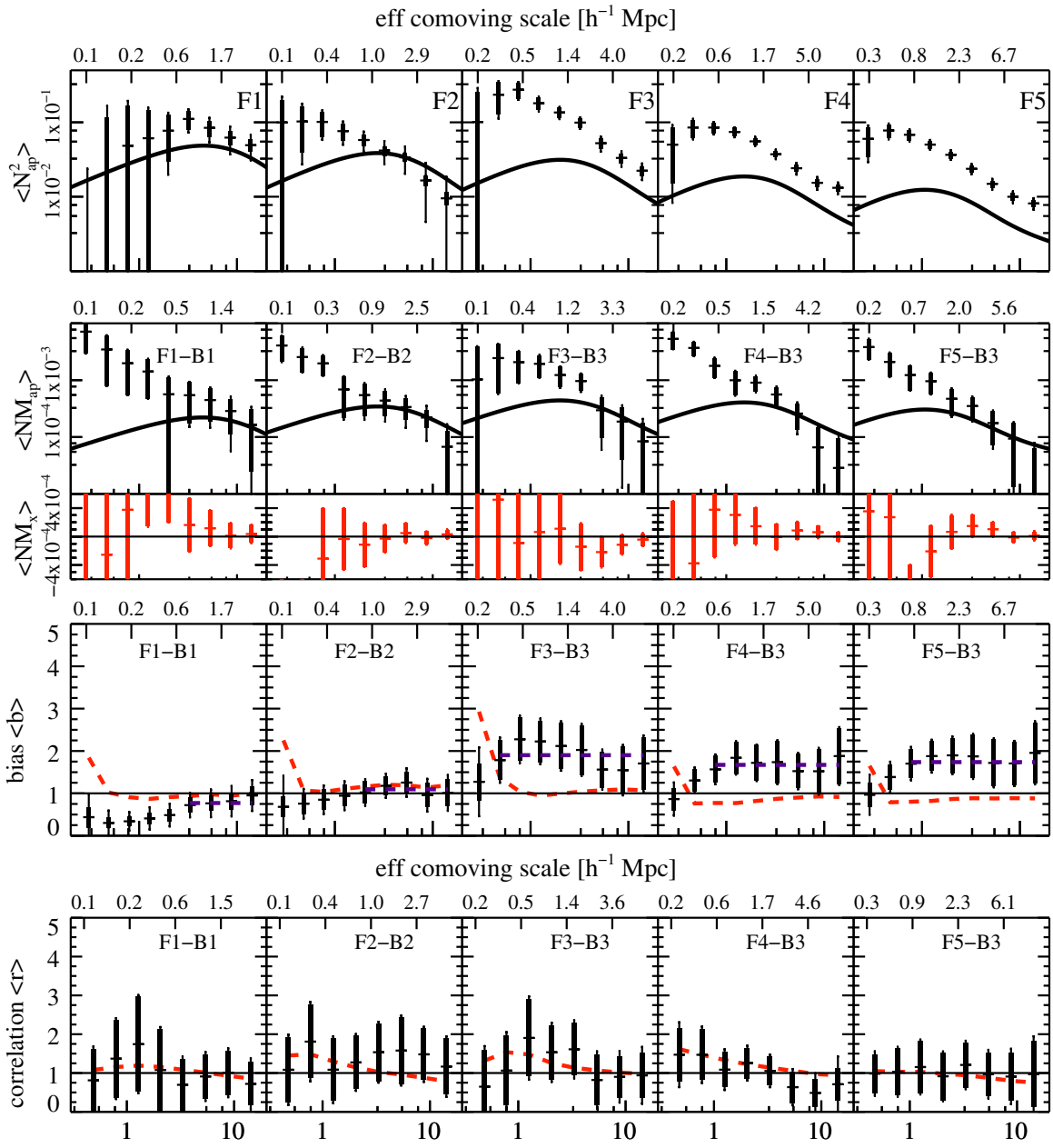

Figure 17. Same as Figure 16, but for galaxies in the stellar mass range $10^{10} < M_* < 10^{11}\,h^{-2}\,M_\odot$.
(A color version of this figure is available in the online journal.)

all around them or the additive systematic is not constant, the average $\langle\gamma_t\rangle$ is biased low. In the SDSS, Mandelbaum et al. (2005) found that subtracting the signal measured around random foreground galaxies was effectively removing this noise. However, our simulations do not include shape noise, and therefore the signal we measure at large scales cannot be due to shape noise.

Another source of systematic error could be related to the tree code we use to compute the correlation functions. The documentation for the tree code Athena mentions that choosing a too large opening angle can smear out the ellipticities of galaxies at large scales. Indeed, we find that if we increase the opening angle, then the effect worsens, but it does not improve with values smaller than the one we use. Because this systematic error is subdominant to our measurements, we decided not to further attempt its correction.

6.2. Bin Mismatch in Redshift

In this section, we show that a mismatch in redshift between peaks of the $p_f(z)$ and the lensing efficiency curves $g(z)$ can alter the bias measurements. We looked into this issue because this is the case in bins F4–B3 and F5–B3. To understand the origin of the problem, we should recall that in our method, the bias is the product of a function f_1 and a measurement $\langle\mathcal{N}^2(\theta)\rangle/\langle M^2_{\rm ap}(\theta)\rangle$.

On the left panel of Figure 18, we compute the ratios $\langle\mathcal{N}^2(\theta)\rangle/\langle M^2_{\rm ap}(\theta)\rangle$ and the inverse of the functions f_1 for different combinations of foreground and background sample bins. We find that between bins F1–B1 and F1–B3 $\langle\mathcal{N}^2(\theta)\rangle/\langle M^2_{\rm ap}(\theta)\rangle$ decreases by 37% and 33% at large and small scales, respectively, whereas function f_1 decreases by 78% and 64%. As a result, our estimations of bias change.

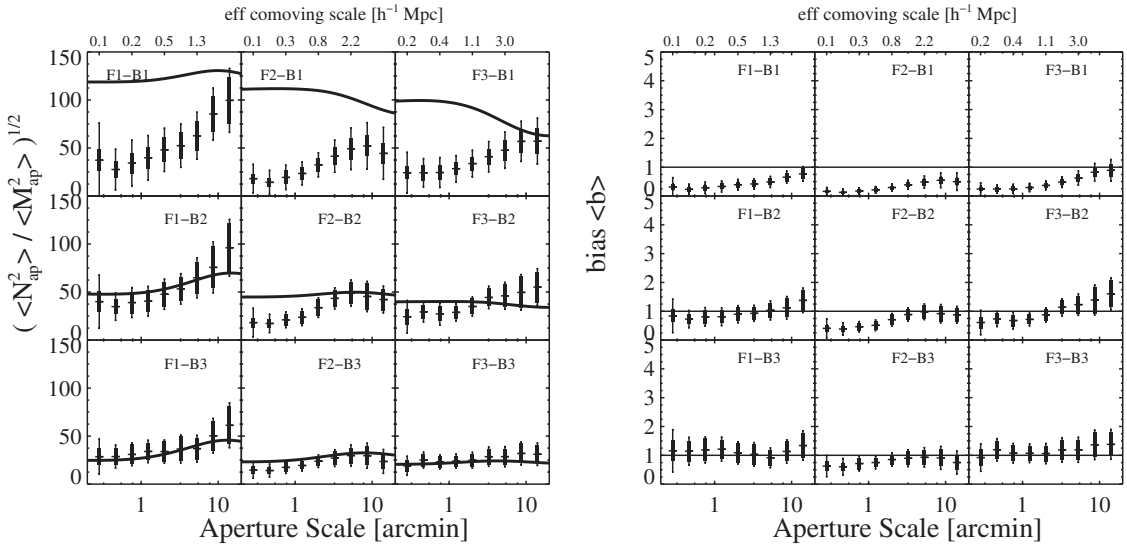

Figure 18. Effects of a mismatch between foreground (F1, F2, F3) and background (B1, B2, B3) redshift bins for the stellar-mass-selected galaxy sample $10^9 < M_* < 10^{10}\,h^{-2}\,M_\odot$. Left panel: the bias parameter $\langle b\rangle$ not calibrated by function $f1$. The thick line is the calibration signal $1/f_1$ computed assuming $b = 1$. Right panel: the bias parameter $\langle b\rangle$ calibrated by function $f1$.

We do expect the signal to decrease because $\langle M^2_{\rm ap}(\theta)\rangle$ increases with redshift, but we do not expect the measured and the predicted signal to change by different amounts. According to Equation (19), the bias measurements should only depend on the foreground redshift distribution, and not on the choice of the background galaxy sample and associated lensing efficiency. This is of course assuming that $\langle M^2_{\rm ap}(\theta)\rangle$ and the matter power spectrum grow linearly, and the lensing-effective matter redshift distribution is well approximated by the lensing efficiency. For very wide surveys where many lines of sight are averaged over, the lensing efficiency might be a good approximation of the effective matter distribution, but in COSMOS, especially at low redshift, this might not be the case. On the other hand, at small scales in the nonlinear regime, the power spectrum might not grow linearly. In Figure 18, smaller scales are more affected by bin mismatch.

Given the limited size of the COSMOS field, we therefore posit that cosmic variance or shape measurements could yield these discrepancies because the volumes probed by $\langle M^2_{\rm ap}(\theta)\rangle$ are too small. These types of discrepancies warn us that for future surveys we should try to match as closely as possible the mean redshift of the foreground galaxies and the peak of the lensing efficiency, in order to limit the effect of cosmic variance.

7. CONCLUSION

The strength of the COSMOS survey is the exceptional quality of the ACS imaging and the 30-band photometry. Thanks to the latter, a photometric redshift can be derived for more than 600,000 galaxies at $I_{814W} < 26.0$ (Ilbert et al. 2009).

In this paper, we made use of these two properties to investigate the evolution of stochastic bias with scale and redshift in COSMOS. We partitioned our foreground galaxy catalogs in three categories: one flux-selected catalog ($I_{814W} < 26.5$ and $K_s < 24$) and two stellar-mass-selected catalogs. To estimate the bias parameter b and the correlation coefficient r, we applied a technique based on aperture statistics described in Schneider (1998) and Hoekstra et al. (2002). We used simulated lensing catalogs derived from N-body simulations to quantify the amount of error due to cosmic variance and to test the method against numerical artifacts. We found that weak-lensing shape noise dominates the error budget and that we are affected by some numerical artifacts at small scales ($\theta < 0.'6$) and at large scales for the correlation coefficient r.

Then, we used a χ^2-test to assess the significance of redshift evolution and scale dependence of bias. We found a significant evolution of bias with redshift but could not confidently rule out an SI model. We found that both bias models proposed by Tinker et al. (2010) and Sheth et al. (2001) provide a good fit to the redshift evolution of our measurements at scales $R > 2\,h^{-1}$ Mpc. We used the result of the fit to derive the halo mass of our stellar-mass-selected galaxy samples. Finally, we observed that bias starts to decline below a scale of about $2\,h^{-1}$ Mpc. We proposed a bias model to describe this scale dependence and obtained a very good fit with $\chi^2/{\rm dof} \leqslant 1$ for our two stellar-mass-selected galaxy samples. We measured a 3σ significance of the turn-down scale $R_{\rm TD}$ for the high stellar mass sample but could not draw conclusions about the evolution of the slope with redshift because of low signal to noise.

Finally, we observed that bias in bins F3–B3 is 2σ off the expectations with a Tinker et al. (2010) bias model. We attribute this to the presence of large overdensities in the COSMOS field already identified in Kovač et al. (2011) and Massey et al. (2007a). With respect to bias stochasticity parameter $\langle r\rangle$, our measurements are all consistent with $\langle r\rangle = 1$. The linear bias model is therefore a good fit to our data, albeit with somewhat large errors.

The COSMOS field is still too small to produce decisive conclusions about the evolution of bias, especially to characterize its scale dependence, and to measure its stochasticity in stellar-mass-selected galaxy samples. On average, we measured signal-to-noise ratios $b/\sigma_b \sim 3$ and $r/\sigma_r \sim 0.5$. The most important source of error is shape noise in the background galaxies. Schneider et al. (1998) have shown that the error on $\langle M^2_{\rm ap}(\theta)\rangle$ decreases as $1/N_b$. In order to increase the signal to noise by a factor of 10, we would need a field 10 times larger.

With their RCS and VIRMOS-DESCART survey of 50.5 deg^2, Hoekstra et al. (2002) obtained signal-to-noise ratios about eight on both bias parameters b and r. However, they did not perform simulations to disentangle systematic and statistical errors as we did in this paper. They also did not have redshift or stellar-mass estimates for their galaxies. Future

ground-based wide-field surveys such as KIDS and VIKING, DES, Pan-STARSS, LSST, and HyperSuprime-Cam on Subaru should provide good photometric redshifts and stellar mass to perform a more conclusive analysis of the scale and redshift dependence of bias.

The main challenge for weak-lensing tomography with the future surveys (this bias analysis being one application) is to measure the shape of background galaxies up to redshift $z = 4$. This is essential to measure the redshift evolution of galaxy properties and bias up to redshift $z \sim 1$. In their current implementation, the space-based missions Euclid and WFIRST propose a near-infrared (NIR) and a visible channel (for Euclid) and very wide field surveys. Visible and NIR imaging is critical to produce good photometric redshifts (Jouvel et al. 2011). These missions will also produce galaxy densities of about 30 arcmin^{-2}. Therefore, with several millions of galaxies, they should be able to measure with good S/N the scale dependence of bias from very small to very large scales.

We thank the referee for his insightful comments that led to a significant improvement of the paper. It is also a pleasure to thank Chris Hirata and Fabian Schmidt for useful discussions and helpful suggestions. We also gratefully thank Alexie Leauthaud for her help and advice and for providing the COSMOS lensing catalog. This work was done in part at JPL, operated by Caltech under a contract for NASA. E.J. acknowledges support from the Jet Propulsion Laboratory, in contract with the California Institute of Technology, and the NASA Postdoctoral Program. R.M. is supported by an STFC Advanced Fellowship.

This work uses observations obtained with the *Hubble Space Telescope*. The HST COSMOS Treasury program was supported through NASA grant HST-GO-09822.

It is also a pleasure to thank Chris Hirata, Fabian Schmidt and Christopher Bonnett for useful discussions and helpful suggestions. Support for Program No. HST-AR-12136.01-A was provided by NASA through a grant from the Space Telescope Science Institute, which is operated by the Association of Universities for Research in Astronomy, Incorporated, under NASA contract NAS5-26555.

APPENDIX A

PRACTICAL ESTIMATORS

In practice, aperture statistics estimators are obtained from two-point correlation functions (Schneider et al. 2002). The correlators used in this work are (1) the angular correlation of the foreground galaxy positions, $\omega(\theta)$, (2) the mean tangential shear about foreground galaxies, $\langle\gamma_t\rangle(\theta)$, and (3) the shear–shear correlation functions $\xi_\pm(\theta)$ as determined from the ellipticities of the background galaxies (Simon et al. 2007).

The angular correlation of the foreground galaxy positions is computed with the Landy & Szalay (1993) estimator defined as

$$\omega(\theta) = \frac{DD}{RR} - 2\frac{DR}{RR} + 1. \tag{A1}$$

The mean tangential shear around foreground galaxies is computed in angular scales and is a function of the shear components γ_1 and γ_2

$$\begin{aligned}\langle\gamma_t\rangle(\theta) &= \left\langle w^{(i)}\gamma_t^{(i,j)}\Delta^{(i,j)}(\theta)\right\rangle \\ &= -\left\langle w^{(i)}\left(\gamma_1^{(i)}\cos 2\phi^{(i,j)} + \gamma_2^{(i)}\sin 2\phi^{(i,j)}\right)\Delta^{(i,j)}\right\rangle,\end{aligned} \tag{A2}$$

where $\phi^{(i,j)} = \theta^{(i)} - \theta^{(j)}$ is the polar angle between foreground galaxy i and background galaxy j. The angle brackets stand for weighted mean over indices i and j and weights $w^{(i)}$. $\Delta^{(i,j)}(\theta)$ is a binning function

$$\Delta^{(i,j)}(\theta) = \begin{cases} 1 & \text{for } \theta \leqslant |\theta_i - \theta_j| < \theta + \delta\theta \\ 0 & \text{otherwise} \end{cases}. \tag{A3}$$

The shear–shear correlation functions $\xi_\pm(\theta)$ are obtained from the correlation of the shear components γ_1 and γ_2:

$$\xi_+(\theta) = \left\langle w^{(i)}w^{(j)}\gamma_1^{(i)}\gamma_1^{(j)}\right\rangle + \left\langle w^{(i)}w^{(j)}\gamma_2^{(i)}\gamma_2^{(j)}\right\rangle\Delta^{(i,j)}(\theta) \tag{A4}$$

$$\begin{aligned}\xi_-(\theta) = \Big(&\left\langle w^{(i)}w^{(j)}\gamma_1^{(i)}\gamma_1^{(j)}\cos 4\phi^{(i,j)}\right\rangle \\ &- \left\langle w^{(i)}w^{(j)}\gamma_2^{(i)}\gamma_2^{(j)}\cos 4\phi^{(i,j)}\right\rangle \\ &+ \left\langle w^{(i)}w^{(j)}\gamma_1^{(i)}\gamma_2^{(j)}\sin 4\phi^{(i,j)}\right\rangle \\ &+ \left\langle w^{(i)}w^{(j)}\gamma_2^{(i)}\gamma_1^{(j)}\sin 4\phi^{(i,j)}\right\rangle\Big)\Delta^{(i,j)}(\theta).\end{aligned} \tag{A5}$$

Aperture statistics estimators can be expressed in terms of these correlators (Schneider et al. 2002; Hoekstra et al. 2002). First, the E- and B-modes of the aperture mass variance $\langle M_{\rm ap}^2(\theta)\rangle$ are obtained from the shear–shear correlation functions $\xi_\pm(\theta)$

$$\left\langle M_{\rm ap}^2(\theta)\right\rangle = \frac{1}{2}\int_0^{2\theta}\frac{d\vartheta\,\vartheta}{\theta^2}\left(\xi_+(\vartheta)T_+\left(\frac{\vartheta}{\theta}\right) + \xi_-(\vartheta)T_-\left(\frac{\vartheta}{\theta}\right)\right), \tag{A6}$$

$$\left\langle M_\perp^2(\theta)\right\rangle = \frac{1}{2}\int_0^{2\theta}\frac{d\vartheta\,\vartheta}{\theta^2}\left(\xi_+(\vartheta)T_+\left(\frac{\vartheta}{\theta}\right) + \xi_-(\vartheta)T_-\left(\frac{\vartheta}{\theta}\right)\right), \tag{A7}$$

where

$$\begin{aligned}T_+(x) = &\frac{6(2-15x^2)}{5}\left[1 - \frac{2}{\pi}\arcsin(x/2)\right] \\ &+ \frac{x\sqrt{4-x^2}}{100\pi}(120 + 2320x^2 - 754^4 \\ &+ 132x^6 - 9x^8),\end{aligned} \tag{A8}$$

$$T_-(x) = \frac{192}{35\pi}x^3\left(1 - \frac{x^2}{4}\right)^{7/2}. \tag{A9}$$

$T_\pm(x)$ vanish for $x > 2$. The B-mode aperture mass $\langle M_\perp^2(\theta)\rangle$ provides a quantitative estimate of the systematics, since gravitational lensing only produces E-modes.

Second, the aperture count variance $\langle\mathcal{N}^2(\theta)\rangle$ is related to $\omega(\theta)$

$$\langle\mathcal{N}^2(\theta)\rangle = \int_0^{2\theta}\frac{d\vartheta\,\vartheta}{\theta^2}\omega(\theta)T_+\left(\frac{\vartheta}{\theta}\right). \tag{A10}$$

Finally, the galaxy-mass cross-correlation aperture $\langle\mathcal{N}(\theta)M_{\rm ap}(\theta)\rangle$ is obtained from the mean tangential shear $\langle\gamma_t\rangle(\theta)$

$$\langle\mathcal{N}(\theta)M_{\rm ap}(\theta)\rangle = \int_0^{2\theta}\frac{d\vartheta\,\vartheta}{\theta^2}\langle\gamma_t\rangle(\theta)F\left(\frac{\vartheta}{\theta}\right), \tag{A11}$$

where the function $F(x)$ has no analytic expression and also vanishes for $x > 2$

$$F(x) = 576\int_0^2\frac{dt}{t}J_2(xt)\left[J_4(t)\right]^2. \tag{A12}$$

APPENDIX B

CORRELATORS

We have seen in Equations (8)–(10) that the aperture statistics $\langle \mathcal{N}^2(\theta)\rangle$, $\langle M_{\rm ap}^2(\theta)\rangle$, and $\langle \mathcal{N}(\theta)M_{\rm ap}(\theta)\rangle$ derive from their respective power spectra multiplied by the same filter function $I(\ell\theta) = J_4(x)/x^2$. This filter is convenient because it is very narrow in Fourier space and almost acts as a $\delta_D(x)$ function. When integrated over the power spectra, it results in very limited correlation between the Fourier modes. The aperture statistics are close approximations of the power spectra but in real space. There is almost a bijective relation between angular scales and Fourier modes. As a result, it is possible to combine the aperture statistics to derive the bias parameters as is done in Fourier space.

In practice, aperture statistics are derived from the correlators $\omega(\theta)$, $\langle\gamma_t\rangle(\theta)$, and $\xi_\pm(\theta)$. Correlators are also derived from the power spectra, but filtered by different filters, as shown below (Hoekstra et al. 2002):

$$\begin{aligned}\omega(\theta) &= \langle\delta n(0)\delta n(\theta)\rangle \\ &= \frac{1}{2\pi}\int_0^\infty d\ell\ \ell\ P_n(\ell)J_0(\ell\theta),\end{aligned} \tag{B1}$$

$$\begin{aligned}\langle\gamma_t\rangle(\theta) &= \langle\delta n(0)\gamma_t(\theta)\rangle \\ &= \frac{1}{2\pi}\int_0^\infty d\ell\ \ell\ P_{\kappa n}(\ell)J_2(\ell\theta),\end{aligned} \tag{B2}$$

$$\begin{aligned}\xi_\pm(\theta) &= \langle\gamma_t(0)\gamma_t(\theta)\rangle \pm \langle\gamma_\times(0)\gamma_\times(\theta)\rangle \\ &= \frac{1}{2\pi}\int_0^\infty d\ell\ \ell\ P_\kappa(\ell)J_{0,4}(\ell\theta).\end{aligned} \tag{B3}$$

Therefore, taking their ratio to derive the bias parameters is unreliable. Note as well that some filters like the Besel function $J_0(x)$ act as low-pass filters. Many Fourier modes are mixed together into one angular scale. Consequently, the correlation between the different angular scales is large.

REFERENCES

Baldauf, T., Smith, R. E., Seljak, U., & Mandelbaum, R. 2010, Phys. Rev. D, 81, 063531
Bertin, E., & Arnouts, S. 1996, A&AS, 117, 393
Blanton, M., Cen, R., Ostriker, J. P., & Strauss, M. A. 1999, ApJ, 522, 590
Bretherton, C., Widmann, M., Dymnikov, V., Wallace, J., & Bladé, I. 1999, J. Clim., 12, 1990
Bundy, K., Scarlata, C., Carollo, C. M., et al. 2010, ApJ, 719, 1969
Capak, P., Aussel, H., Ajiki, M., et al. 2007, ApJS, 172, 99
Coil, A. L., Newman, J. A., Croton, D., et al. 2008, ApJ, 672, 153
Coupon, J., Kilbinger, M., McCracken, H. J., et al. 2011, arXiv:1107.0616
Cresswell, J. G., & Percival, W. J. 2009, MNRAS, 392, 682
de la Torre, S., Guzzo, L., Kovač, K., et al. 2010, MNRAS, 409, 867
Dekel, A., & Lahav, O. 1999, ApJ, 520, 24
Efstathiou, G., Bernstein, G., Tyson, J. A., Katz, N., & Guhathakurta, P. 1991, ApJ, 380, L47
Eisenstein, D. J., & Hu, W. 1999, ApJ, 511, 5
Finoguenov, A., Guzzo, L., Hasinger, G., et al. 2007, ApJS, 172, 182
Guzzo, L., Cassata, P., Finoguenov, A., et al. 2007, ApJS, 172, 254
Hilbert, S., Hartlap, J., White, S. D. M., & Schneider, P. 2009, A&A, 499, 31
Hoekstra, H., van Waerbeke, L., Gladders, M. D., Mellier, Y., & Yee, H. K. C. 2002, ApJ, 577, 604
Hoekstra, H., Yee, H. K. C., & Gladders, M. D. 2001, ApJ, 558, L11
Ilbert, O., Capak, P., Salvato, M., et al. 2009, ApJ, 690, 1236
Joachimi, B., Schneider, P., & Eifler, T. 2008, A&A, 477, 43
Johnston, D. E., Sheldon, E. S., Wechsler, R. H., et al. 2007, arXiv:0709.1159
Jouvel, S., Kneib, J.-P., Bernstein, G., et al. 2011, A&A, 532, A25
Kiessling, A., Heavens, A. F., Taylor, A. N., & Joachimi, B. 2011, MNRAS, 414, 2235
Kilbinger, M., Schneider, P., & Eifler, T. 2006, A&A, 457, 15
Koekemoer, A. M., Aussel, H., Calzetti, D., et al. 2007, ApJS, 172, 196
Komatsu, E., Smith, K. M., Dunkley, J., et al. 2011, ApJS, 192, 18
Kovač, K., Porciani, C., Lilly, S. J., et al. 2011, ApJ, 731, 102
Kravtsov, A. V., Berlind, A. A., Wechsler, R. H., et al. 2004, ApJ, 609, 35
Landy, S. D., & Szalay, A. S. 1993, ApJ, 412, 64
Leauthaud, A., Massey, R., Kneib, J.-P., et al. 2007, ApJS, 172, 219
Leauthaud, A., Tinker, J., Behroozi, P. S., Busha, M. T., & Wechsler, R. 2011, ApJ, 738, 45
Leauthaud, A., Tinker, J., Bundy, K., et al. 2012, ApJ, 744, 159
Lilly, S. J., Le Brun, V., Maier, C., et al. 2009, ApJS, 184, 218
Mandelbaum, R., Hirata, C. M., Seljak, U., et al. 2005, MNRAS, 361, 1287
Marinoni, C., Le Fèvre, O., Meneux, B., et al. 2005, A&A, 442, 801
Massey, R., Rhodes, J., Ellis, R., et al. 2007a, Nature, 445, 286
Massey, R., Rhodes, J., Leauthaud, A., et al. 2007b, ApJS, 172, 239
Massey, R., Stoughton, C., Leauthaud, A., et al. 2010, MNRAS, 401, 371
McCracken, H. J., Capak, P., Salvato, M., et al. 2010, ApJ, 708, 202
McCracken, H. J., Peacock, J. A., Guzzo, L., et al. 2007, ApJS, 172, 314
Meneux, B., Guzzo, L., de la Torre, S., et al. 2009, A&A, 505, 463
Meneux, B., Le Fèvre, O., Guzzo, L., et al. 2006, A&A, 452, 387
Nelder, J. A., & Mead, R. 1965, Comput. J., 7, 308
Neyrinck, M. C., Hamilton, A. J. S., & Gnedin, N. Y. 2005, MNRAS, 362, 337
Ouchi, M., Hamana, T., Shimasaku, K., et al. 2005, ApJ, 635, L117
Peacock, J. A., & Dodds, S. J. 1996, MNRAS, 280, L19
Peng, Y., Lilly, S. J., Renzini, A., & Carollo, M. 2011, arXiv:1106.2546
Rhodes, J., Refregier, A., & Groth, E. J. 2000, ApJ, 536, 79
Schneider, P. 1998, ApJ, 498, 43
Schneider, P., van Waerbeke, L., Jain, B., & Kruse, G. 1998, MNRAS, 296, 873
Schneider, P., van Waerbeke, L., Kilbinger, M., & Mellier, Y. 2002, A&A, 396, 1
Scoville, N., Aussel, H., Brusa, M., et al. 2007, ApJS, 172, 1
Sheldon, E. S., Johnston, D. E., Frieman, J. A., et al. 2004, AJ, 127, 2544
Sheth, R. K., Mo, H. J., & Tormen, G. 2001, MNRAS, 323, 1
Sheth, R. K., & Tormen, G. 1999, MNRAS, 308, 119
Simon, P. 2007, A&A, 473, 711
Simon, P., Hetterscheidt, M., Schirmer, M., et al. 2007, A&A, 461, 861
Smith, R. E., Peacock, J. A., Jenkins, A., et al. 2003, MNRAS, 341, 1311
Somerville, R. S., Lemson, G., Sigad, Y., et al. 2001, MNRAS, 320, 289
Tegmark, M., & Bromley, B. C. 1999, ApJ, 518, L69
Tinker, J., Kravtsov, A. V., Klypin, A., et al. 2008, ApJ, 688, 709
Tinker, J. L., Robertson, B. E., Kravtsov, A. V., et al. 2010, ApJ, 724, 878
van Waerbeke, L. 1998, A&A, 334, 1
van Waerbeke, L., Bernardeau, F., & Mellier, Y. 1999, A&A, 342, 15
Weinberg, N. N., & Kamionkowski, M. 2003, MNRAS, 341, 251
Wild, V., Peacock, J. A., Lahav, O., et al. 2005, MNRAS, 356, 247
Yoshikawa, K., Taruya, A., Jing, Y. P., & Suto, Y. 2001, ApJ, 558, 520
Zehavi, I., Eisenstein, D. J., Nichol, R. C., et al. 2005, ApJ, 621, 22
Zehavi, I., Zheng, Z., Weinberg, D. H., et al. 2011, ApJ, 736, 59
Zheng, Z., Zehavi, I., Eisenstein, D. J., Weinberg, D. H., & Jing, Y. P. 2009, ApJ, 707, 554